HAT-P-58b–HAT-P-64b: Seven Planets Transiting Bright Stars[*]

G. Á. Bakos,[1,2,†] J. D. Hartman,[1] W. Bhatti,[1] Z. Csubry,[1] K. Penev,[3] A. Bieryla,[4] D. W. Latham,[4] S. Quinn,[4]
L. A. Buchhave,[5] G. Kovács,[6] Guillermo Torres,[4] R. W. Noyes,[4] E. Falco,[4] Bence Béky,[7] T. Szklenár,[6]
G. A. Esquerdo,[4] A. W. Howard,[8] H. Isaacson,[9] G. Marcy,[9] B. Sato,[10] I. Boisse,[11] A. Santerne,[11] G. Hébrard,[12]
M. Rabus,[13,14] D. Harbeck,[13] C. McCully,[13] M. E. Everett,[15] E. P. Horch,[16] L. Hirsch,[17] S. B. Howell,[18]
C. X. Huang,[19] J. Lázár,[20] I. Papp,[20] and P. Sári[20]

[1]Department of Astrophysical Sciences, Princeton University, NJ 08544, USA
[2]MTA Distinguished Guest Fellow, Konkoly Observatory, Research Centre for Astronomy and Earth Sciences, H-1121 Budapest, Konkoly Thege Mikls t 15-17, Hungary
[3]Department of Physics, University of Texas at Dallas, Richardson, TX 75080, USA
[4]Center for Astrophysics | Harvard & Smithsonian, 60 Garden St, Cambridge, MA 02138, USA
[5]DTU Space, National Space Institute, Technical University of Denmark, Elektrovej 328, DK-2800 Kgs. Lyngby, Denmark
[6]Konkoly Observatory, Research Centre for Astronomy and Earth Sciences, H-1121 Budapest, Konkoly Thege Mikls t 15-17, Hungary
[7]Google, Googleplex, 1600 Amphitheatre Parkway, Mountain View, CA 94043, USA
[8]Department of Astronomy, California Institute of Technology, Pasadena, CA, USA
[9]Department of Astronomy, University of California, Berkeley, CA, USA
[10]Department of Earth and Planetary Sciences, Tokyo Institute of Technology, 2-12-1 Ookayama, Meguro-ku, Tokyo 152-8551, Japan
[11]Aix Marseille Université, CNRS, LAM (Laboratoire d'Astrophysique de Marseille) UMR 7326, F-13388, Marseille, France
[12]Institut d'Astrophysique de Paris, UMR7095 CNRS, Université Pierre & Marie Curie, 98bis boulevard Arago, 75014 Paris, France
[13]Las Cumbres Observatory Global Telescope Network, 6740 Cortona Dr. Suite 102, Goleta, CA 93117
[14]Department of Physics, University of California, Santa Barbara, CA 93106-9530, USA
[15]NSF's Optical-Infrared Astronomy Research Lab, Tucson, AZ 85719 USA
[16]Department of Physics, Southern Connecticut State University, 501 Crescent Street, New Haven, CT 06515, USA
[17]Kavli Institute for Particle Astrophysics and Cosmology, Stanford University, Stanford, CA, USA
[18]NASA Ames Research Center, Moffett Field, CA, 94035, USA
[19]Department of Physics, and Kavli Institute for Astrophysics and Space Research, Massachusetts Institute of Technology, Cambridge, MA 02139, USA
[20]Hungarian Astronomical Association, 1451 Budapest, Hungary

ABSTRACT

We report the discovery and characterization of 7 transiting exoplanets from the HATNet survey. The planets, which are hot Jupiters and Saturns transiting bright sun-like stars, include: HAT-P-58b (with mass $M_p = 0.37 M_J$, radius $R_p = 1.33 R_J$, and orbital period $P = 4.0138$days), HAT-P-59b ($M_p = 1.54 M_J$, $R_p = 1.12 R_J$, $P = 4.1420$days), HAT-P-60b ($M_p = 0.57 M_J$, $R_p = 1.63 R_J$, $P = 4.7948$days), HAT-P-61b ($M_p = 1.06 M_J$, $R_p = 0.90 R_J$, $P = 1.9023$days), HAT-P-62b ($M_p = 0.76 M_J$, $R_p = 1.07 R_J$, $P = 2.6453$days), HAT-P-63b ($M_p = 0.61 M_J$, $R_p = 1.12 R_J$, $P = 3.3777$days), and HAT-P-64b ($M_p = 0.58 M_J$, $R_p = 1.70 R_J$, $P = 4.0072$days). The typical errors on these quantities are $0.06 M_J$, $0.03 R_J$, and 0.2seconds, respectively. We also provide accurate stellar parameters for each of the hosts stars. With $V = 9.710 \pm 0.050$mag, HAT-P-60 is an especially bright transiting planet host, and an excellent target for additional follow-up observations. With $R_p = 1.703 \pm 0.070 R_J$, HAT-P-64b is a highly inflated hot Jupiter around a star nearing the end of its main-sequence lifetime, and is among the largest known planets. Five of the seven systems have long-cadence observations by *TESS*

Corresponding author: Gáspár Bakos

gbakos@astro.princeton.edu

which are included in the analysis. Of particular note is HAT-P-59 (TOI-1826.01) which is within the Northern continuous viewing zone of the *TESS* mission, and HAT-P-60, which is the TESS candidate TOI-1580.01.

1. INTRODUCTION

The Hungarian-made Automated Telescope Network (HATNet; Bakos et al. 2004) began initial operations in 2003, with the primary science goal of discovering and accurately characterizing transiting extrasolar planets (TEPs) around bright stars. It is one of four ongoing ground-based wide field transiting planet surveys with more than ten planet discoveries, the others being HAT-South (Bakos et al. 2013, although led by the same PI, this project is independent from the northern HATNet survey), SuperWASP (Pollacco et al. 2006) and KELT (Pepper et al. 2007).

HATNet consists of six 11 cm diameter telephoto lenses coupled to front-side-illuminated charged-coupled device (CCD) imagers, each in a separate mount and enclosure. Four of the units (called HAT-5, -6, -7, and -10) are located at Fred Lawrence Whipple Observatory (FLWO) in Arizona, while the other two (called HAT-8 and -9) are located on the roof of the Submillimeter Array service building at Mauna Kea Observatory (MKO) in Hawaii. The system has been fully operational in an autonomous fashion since 2004, and has remained nearly homogenous, with only a few changes to the instrumentation and observing procedures since that time. To date a total of 63 TEP discoveries have been published based on HATNet observations (the most recent being Zhou et al. 2019). Here we present the discovery of 7 new TEP systems identified using HATNet, together with an accurate determination of the system parameters, including precise radial velocity (RV) observations used to measure the planetary masses. Before delving into a detailed discussion of these new discoveries, we first provide a brief update on the status of HATNet.

Since 2004 there have been four different combinations of CCD cameras and filters used by HATNet. The initial setup (until the summer of 2007) made use of Apogee AP10 $2K \times 2K$ CCDs and Cousins I-band filters. This provided a $8°.2 \times 8°.2$ field of view (FOV) and a plate scale of $14''$ pixel^{-1}. In September 2007 we replaced the CCDs to Apogee U16m $4K \times 4K$ imagers, providing a larger

field of view ($10°.6 \times 10°.6$) and higher spatial resolution ($9''$ pixel^{-1}). We also changed the filters to Bessel R-band to better match the peak QE of the CCD, and a year later (in September 2008), we changed the filters to Sloan r band to have better overall response, and sharp wavelength boundaries. Majority of the HATNet survey was performed with this setup, i.e. the Apogee U16m $4K \times 4K$ imagers and the Sloan r band filters. The most recent modification was in October 2013, when the imager on HAT-7 at FLWO was changed to an FLI back-side-illuminated $2K \times 2K$ CCD device. The other units continue to use the Apogee U16m $4K \times 4K$ devices.

HATNet follows a point-and-stare mode of observations, where each unit is assigned a primary field (one of 838 discrete pointings which tile the full 4π steradian celestial sphere), which it observes continuously over the night using 3 min integrations, so long as the field is above $30°$ elevation, and not too close to the moon. A secondary field is also assigned to each instrument, which is observed when the primary field is not visible. In recent years we have adopted a strategy where all of the units are assigned the same primary and secondary fields, which we have found to significantly increase the sensitivity to small radius planets. This is in contrast to our earlier mode of observing where different units are assigned different fields to maximize the sky coverage. The total time spent on a field varies significantly, from a minimum of 2,000 observations, to as many as 40,000 observations collected (the median is 6000 observations). As of May 2020, a total of 185 fields, corresponding to 148 unique pointing positions[1], and covering approximately 35% of the Northern sky, have been observed, reduced, and searched for transiting planets. Some 9.3 million light curves have been generated from these images for 5.9 million stars ranging in brightness from $r \approx 9.5$ mag to $r = 14.5$. The trend-filtered light curves reach a precision of ~ 3 mmag at cadence for the brightest sources. Based on these light curves a total of 2460 candidate transiting planets have been selected.

---

[1] We have revisited some sky positions with a different instrumental configuration leading to multiple "fields" for these positions.

$\dagger$ Packard Fellow

The majority of the candidates (approximately 2200 to date) have received at least some follow-up spectroscopic and/or photometric observations using a variety of facilities (e.g., Latham et al. 2009). Based on these observations, some 1950 of the candidates have been set aside as false positives or false alarms (i.e., cases where we suspect that the candidate transit signal detected in the HATNet light curve is spurious). In addition to those planets presented here, more than a dozen other planets have been confirmed, but have not yet been published. Some 250 candidates have received some follow-up, but require additional follow-up observations for confirmation and characterization.

The seven planets that are the focus of this paper are quite typical of the population of transiting planets that have been discovered thus far by HATNet. With planetary masses between $0.372 \pm 0.030\,M_{\rm J}$ (HAT-P-58b) and $1.540 \pm 0.067\,M_{\rm J}$ (HAT-P-59b), orbital periods between 1.9023 days (HAT-P-61b) and 4.7948 days (HAT-P-60b), and host star masses between $0.925 \pm 0.023\,M_\odot$ (HAT-P-63) and $1.298 \pm 0.021\,M_\odot$ (HAT-P-64), these are all hot Jupiters transiting Sun-like stars. The host stars are all relatively bright, particularly HAT-P-60 at $V = 9.710 \pm 0.050$ mag, enabling the accurate determination of the orbital parameters, and planetary and stellar physical parameters, that we provide in this paper for each of these systems. The targets are also amenable to additional follow-up observations that may be carried out to characterize the orbital geometries (e.g., spin–orbit alignment measurements via the Rossiter-McLaughlin effect, Queloz et al. 2000) and planetary atmospheres (e.g., transmission spectroscopy, Charbonneau et al. 2002). The continued discovery and characterization of TEPs such as these increases the sample that may be used for statistical analysis of the population, which in turn provides insights into the physical processes involved in their formation and evolution. In fact, the planets reported here have already been included in a statistical analysis carried out by Hartman et al. (2016), which revealed observational evidence for the re-inflation of close-in giant planets.

In the next section (2) we describe the observations collected to identify, confirm, and characterize the seven transiting planet systems presented here. The analysis carried out to measure the parameters of each system and to rule out blended stellar eclipsing binary false positive scenarios is described in Section 3. We discuss the results in Section 4.

2. OBSERVATIONS

2.1. Photometric detection

Periodic transit events were first identified for all seven systems based on time series photometric observations obtained with the HATNet wide-field photometric network (Bakos et al. 2004). The instruments and filters used, number of measurements collected and date range over which they were collected, observational cadence, and photometric precision achieved are all listed in Tables 1 and 2 for each of the seven systems. The raw HATNet images were reduced to light curves following Bakos et al. (2004), making use of aperture and image subtraction photometry routines based on the FITSH software package Pál (2012). Following Bakos et al. (2010) we filtered variations from the light curves that are correlated with a variety of auxiliary parameters, and we then applied the Trend-Filtering Algorithm (TFA) of Kovács et al. (2005). The latter operates by fitting each light curve as a linear combination of "template" light curves (in our case these are light curves for a random sample of non-variable stars distributed across the image plane and in magnitude) and then subtracting the best fit model from the light curve being filtered. In our initial pass we apply the filtering in signal recovery mode, where we assume the light curve contains no astrophysical variations. We then use the Box Least Squares (BLS; Kovács et al. 2002) method to search the filtered light curves for periodic transits. Once recovered, we then re-apply the trend filtering, this time in signal reconstruction mode, where we simultaneously fit to the light curve the linear filter and a periodic box-shaped transit model. This produced a filtered light curve without distorting the transit signal. The final trend-filtered photometric data for each system are shown phase-folded in Figure 1, and Figures 5–10, while the measurements are available in Table 5.

We used the VARTOOLS package (Hartman & Bakos 2016) to search the residual HATNet light curves of each target for additional periodic transit signals using BLS, but do not find any significant signals attributable to additional transiting planets around these stars. For HAT-P-58 the highest peak in the BLS spectrum (in the residual light curve) is at $P = 38.5$ d with a signal-to-pink noise ratio (S/N$_{\rm pink}$) of 5.5 (we require S/N$_{\rm pink} > 7.0$ for detection) and a transit depth of 6.3 mmag. For HAT-P-59 we detect a signal at the sidereal frequency, which is presumably due to systematic errors in the photometry that are not fully removed through EPD and TFA. The first harmonic of this same signal is also detected with the Generalized Lomb-Scargle periodogram (GLS; Zechmeister & Kürster 2009), and when it is filtered from the light curve using a Fourier series fit, we find no other significant transit signals with BLS. Altogether, we find the

following peaks, significances and transit depths in the residual light curves:

- HAT-P-58, $P = 38.5$ d, S/N$_{pink} = 5.5$, 6.3 mmag;

- HAT-P-59, $P = 1.59$ d, S/N$_{pink} = 6.0$, 2.3 mmag;

- HAT-P-60, $P = 2.48$ d, S/N$_{pink} = 6.1$, 2.3 mmag;

- HAT-P-61, $P = 61.8$ d, S/N$_{pink} = 5.2$, 2.7 mmag;

- HAT-P-62, $P = 0.146$ d, S/N$_{pink} = 6.1$, 2.9 mmag;

- HAT-P-63, $P = 0.194$ d, S/N$_{pink} = 6.0$, 8.3 mmag;

- HAT-P-64, $P = 0.438$ d, S/N$_{pink} = 6.7$, 2.3 mmag;

We also used VARTOOLS to search the residual HAT-Net light curves for continuous periodic variability with GLS. For HAT-P-58, HAT-P-60, and HAT-P-62–HAT-P-64 we do not detect any periodic signals, and place 95% confidence upper limits on the peak-to-peak amplitudes of such signals of 2.0 mmag for HAT-P-58, 0.96 mmag for HAT-P-60, 1.2 mmag for HAT-P-62, 3.9 mmag for HAT-P-63, and 2.0 mmag for HAT-P-64. For HAT-P-59 a strong signal with a period of $P = 0.49976 \pm 0.00086$ days is detected with a peak-to-peak amplitude of 16.6 mmag. Given the close proximity of the period to twice the sidereal frequency, we suspect that this signal is most likely be due to systematic errors in the photometry that are not fully corrected through EPD and TFA. After subtracting a Fourier series model from the light curve, GLS finds no additional signals present in the data, and we place a 95% confidence upper limit of 1.5 mmag on the peak-to-peak amplitude of any such signals. For HAT-P-61 we detect a possible signal with a period of 10.6 ± 0.5 days and with a formal false alarm probability of 0.16% and peak-to-peak amplitude of 2.6 mmag. The GLS periodogram is shown in Figure 3. This may correspond to the photometric rotation period of the star, in which case the equatorial rotation velocity of 4.7 km s^{-1} is 2σ larger than the spectroscopically measured projected rotation velocity of $v \sin i = 3.69 \pm 0.50$ km s^{-1}.

2.2. *Spectroscopic Observations*

Spectroscopic observations of the TEP systems were carried out using the Tillinghast Reflector Echelle Spectrograph (TRES; Fűrész 2008) on the 1.5 m Tillinghast Reflector at FLWO, the SOPHIE spectrograph (Bouchy et al. 2009) on the Observatoire de Haute Provence (OHP) 1.93 m in France, HIRES (Vogt et al. 1994) on the Keck-I 10 m at MKO together with its I$_2$ absorption cell, the High Dispersion Spectrograph (HDS; Noguchi et al. 2002) and its I$_2$ cell (Kambe et al. 2002) on

the Subaru 8 m at MKO, the Astrophysical Research Consortium Echelle Spectrometer (ARCES; Wang et al. 2003) on the ARC 3.5 m telescope at Apache Point Observatory (APO) in New Mexico, the FIbre-fed Échelle Spectrograph (FIES) on the Nordic Optical Telescope (NOT) 2.5 m (Djupvik & Andersen 2010) in La Palma, Spain, and the Network of Robotic Echelle Spectrographs (NRES; Siverd et al. 2018) on the LCOGT 1 m network. Table 3 summarizes the spectroscopic observations collected for each TEP system. Phased high-precision RV and bisector (BS) measurements are shown for each system in Figures 1–10. The data are listed in Table 12 at the end of the paper.

The TRES observations were reduced to spectra and cross-correlated against synthetic stellar templates to measure the RVs and to estimate $T_{eff\star}$, $\log g$, and $v \sin i$. Here we followed the procedure of Buchhave et al. (2010), initially making use of a single order containing the gravity and temperature-sensitive Mg b lines. Based on these observations we quickly ruled out common false positive scenarios, such as transiting M dwarf stars, or blends between giant stars and pairs of eclipsing dwarf stars. For HAT-P-59 through HAT-P-63 the initial TRES RVs exhibited low amplitude variations consistent with planetary mass companions, so we continued to collect spectroscopic observations with TRES for these objects with the aim of confirming them as TEP systems, measuring the masses of the planets, and providing high precision stellar atmospheric parameters, including the stellar metallicities. For this work high precision RVs and spectral line bisector spans (BSs) were determined based on a multi-order analysis of the spectra (e.g., Bieryla et al. 2014), while the atmospheric parameters were determined using the Stellar Parameter Classification (SPC; Buchhave et al. 2012) method. For HAT-P-58 and HAT-P-64 the TRES observations were used solely for reconnaissance and were not included in the analysis described in Section 3.3.

The SOPHIE observations of HAT-P-59, HAT-P-60, HAT-P-63 and HAT-P-64 were reduced to RVs and BSs following Boisse et al. (2013). In all cases the RVs show variations consistent with planetary mass companions, and with the variations seen using other spectrographs.

The HIRES observations of HAT-P-58, HAT-P-60, HAT-P-61, and HAT-P-64 were reduced to relative RVs following the method of Butler et al. (1996), and to BSs following Torres et al. (2007). We also measured Ca II HK chromospheric emission indices (the so-called S and $\log_{10} R'_{HK}$ indices) following Isaacson & Fischer (2010) and Noyes et al. (1984). For HAT-P-64 we measured stellar atmospheric parameters from the I$_2$-free template spectra using SPC.
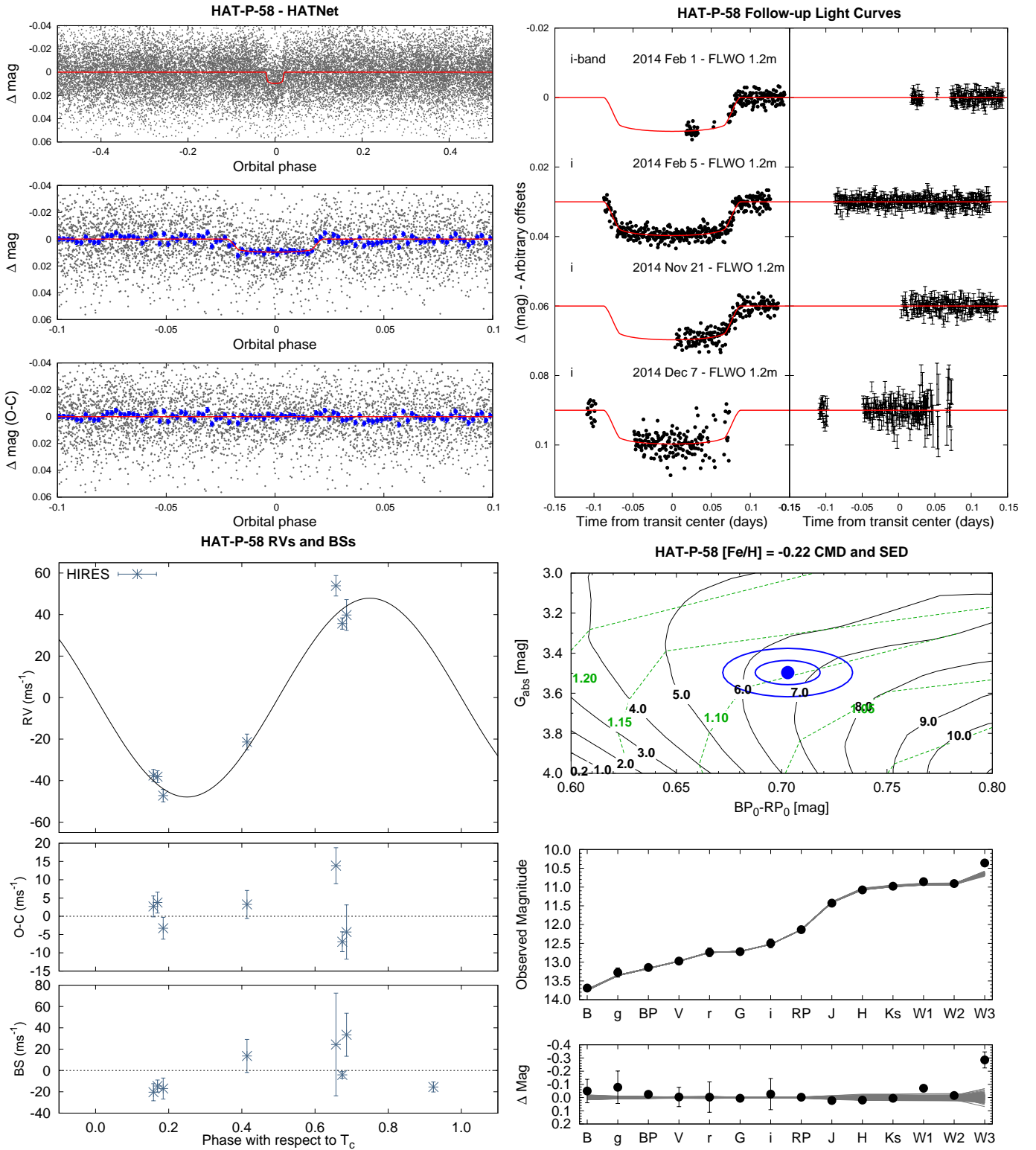
Figure 1. Observations used to confirm the transiting planet system HAT-P-58, excluding data from the NASA *TESS* mission which are shown in Figure 2. *Top Left:* Phase-folded unbinned HATNet light curve. The top panel shows the full light curve, the middle panel shows the light curve zoomed-in on the transit, and the bottom panel shows the residuals from the best-fit model zoomed-in on the transit. The solid lines show the model fits to the light curves. The dark filled circles show the light curves binned in phase with a bin size of 0.002. (Caption continued on next page.)

Figure 1. (Caption continued from previous page.) *Top Right:* Unbinned follow-up transit light curves corrected for instrumental trends fitted simultaneously with the transit model, which is overplotted. The dates, filters and instruments used are indicated. The residuals are shown on the right-hand-side in the same order as the original light curves. The error bars represent the photon and background shot noise, plus the readout noise. Note that these uncertainties are scaled up in the fitting procedure to achieve a reduced χ^2 of unity, but the uncertainties shown in the plot have not been scaled. *Bottom Left:* High-precision RVs phased with respect to the mid-transit time. The instruments used are labelled in the plot. The top panel shows the phased measurements together with the best-fit model. The center-of-mass velocity has been subtracted. The second panel shows the velocity $O-C$ residuals. The error bars include the estimated jitter. The third panel shows the bisector spans. *Bottom Right:* Color-magnitude diagram (CMD) and spectral energy distribution (SED). The top panel shows the absolute G magnitude vs. the de-reddened $BP - RP$ color compared to theoretical isochrones (black lines) and stellar evolution tracks (green lines) from the PARSEC models interpolated at the best-estimate value for the metallicity of the host. The age of each isochrone is listed in black in Gyr, while the mass of each evolution track is listed in green in solar masses. The filled blue circles show the measured reddening- and distance-corrected values from Gaia DR2, while the blue lines indicate the 1σ and 2σ confidence regions, including the estimated systematic errors in the photometry. Note that the determination of the final age of the system is informed by other input parameters, such as the spectroscopic effective temperature, the broad-band photometry in additional bandpasses and the stellar density from the light curves. The middle panel shows the SED as measured via broadband photometry through the listed filters. Here we plot the observed magnitudes without correcting for distance or extinction. Overplotted are 200 model SEDs randomly selected from the MCMC posterior distribution produced through the global analysis (gray lines). The model makes use of the predicted absolute magnitudes in each bandpass from the PARSEC isochrones, the distance to the system (constrained largely via Gaia DR2) and extinction (constrained from the SED with a prior coming from the MWDUST 3D Galactic extinction model). The bottom panel shows the $O-C$ residuals from the best-fit model SED.
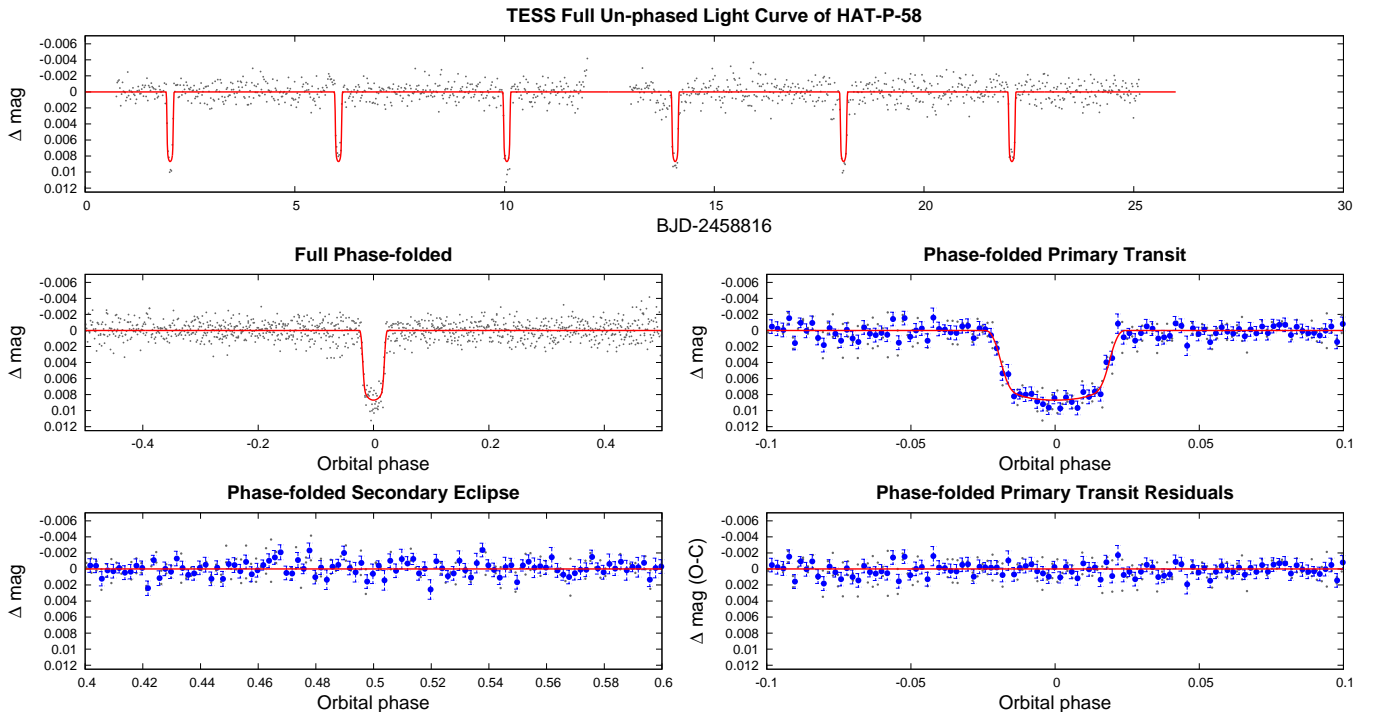
Figure 2. *TESS* long-cadence light curve for HAT-P-58. We show the full un-phased light curve as a function of time (*top*), the full phase-folded light curve (*middle left*), the phase-folded light curve zoomed-in on the planetary transit (*middle right*), the phase-folded light curve zoomed-in on the secondary eclipse (*bottom left*), and the residuals from the best-fit model, phase-folded and zoomed-in on the planetary transit (*bottom right*). The solid line in each panel shows the model fit to the light curve, account for the 30 min integrations. The dark filled circles show the light curve binned in phase with a bin size of 0.002. Other observations included in our analysis of this system are shown in Figure 1.

Table 1. Summary of photometric observations HAT-P-58–HAT-P-61

Instrument/Field[a]	Date(s)	# Images[b]	Cadence[c] (sec)	Filter	Precision[d] (mmag)
HAT-P-58					
HAT-5/G093	2012 Sep–2013 Apr	9254	213	r	21.3
HAT-7/G093	2012 Sep	238	213	r	18.3
HAT-8/G093	2012 Jul–2013 Apr	11078	217	r	14.8
FLWO 1.2 m/KeplerCam	2014 Feb 01	157	48	i	1.5
FLWO 1.2 m/KeplerCam	2014 Feb 05	378	48	i	1.5
FLWO 1.2 m/KeplerCam	2014 Nov 21	207	51	i	1.8
FLWO 1.2 m/KeplerCam	2014 Dec 07	188	51	i	3.1
TESS/Sector 19	2019 Nov 29–2019 Dec 23	1117	1798	T	1.1
HAT-P-59					
HAT-5/G081	2012 Oct–2012 Dec	1963	213	r	11.1
HAT-6/G081	2012 Sep–2012 Dec	2500	214	r	9.1
HAT-7/G081	2012 Jul–2012 Dec	2340	213	r	9.3
HAT-8/G081	2012 Sep–2012 Dec	2121	214	r	9.1
HAT-9/G081	2012 Sep–2012 Dec	2158	213	r	8.1
FLWO 1.2 m/KeplerCam	2013 Nov 12	189	26	i	2.9
FLWO 1.2 m/KeplerCam	2014 Feb 19	177	26	i	2.5
FLWO 1.2 m/KeplerCam	2014 Mar 16	314	27	i	2.1
FLWO 1.2 m/KeplerCam	2014 May 13	642	26	i	2.5
TESS/Sector 14	2019 Jul 18–2019 Aug 14	1233	1799	T	0.75
TESS/Sector 15	2019 Aug 15–2019 Sep 8	821	1799	T	0.72
TESS/Sector 16	2019 Sep 12–2019 Oct 6	999	1799	T	0.66
TESS/Sector 17	2019 Oct 8–2019 Oct 31	938	1799	T	0.64
TESS/Sector 18	2019 Nov 4–2019 Nov 27	1036	1799	T	0.63
TESS/Sector 20	2019 Dec 25–2020 Jan 20	1175	1799	T	0.66
TESS/Sector 21	2020 Jan 23–2020 Feb 18	1189	1799	T	0.72
HAT-P-60					
HAT-7/G089	2009 Sep–2010 Mar	5577	225	r	4.4
FLWO 1.2 m/KeplerCam	2013 Oct 20	873	25	z	3.6
FLWO 1.2 m/KeplerCam	2014 Sep 11	840	22	i	2.9
FLWO 1.2 m/KeplerCam	2014 Oct 10	781	22	z	2.9
TESS/Sector 18	2019 Nov 4–2019 Nov 27	1031	1799	T	0.38
HAT-P-61					
HAT-5/G094	2007 Oct–2008 Mar	3526	384	R	11.2
HAT-5/G093	2012 Sep–2013 Apr	9476	213	r	18.6
HAT-7/G093	2012 Sep	240	213	r	17.3
HAT-8/G093	2012 Jul–2013 Apr	11084	217	r	15.6
FLWO 1.2 m/KeplerCam	2014 Sep 21	165	58	i	1.5
FLWO 1.2 m/KeplerCam	2014 Oct 10	280	59	i	2.4
TESS/Sector 19	2019 Nov 28–2019 Dec 23	1145	1799	T	1.1

[a] For HATNet data we list the HATNet unit and field name from which the observations are taken. HAT-5, -6, -7 and -10 are located at Fred Lawrence Whipple Observatory in Arizona. HAT-8 and -9 are located on the roof of the Smithsonian Astrophysical Observatory Submillimeter Array hangar building at Mauna Kea Observatory in Hawaii. Each field corresponds to one of 838 fixed pointings used to cover the full 4π celestial sphere. All data from a given HATNet field are reduced together, while detrending through External Parameter Decorrelation (EPD) is done independently for each unique unit+field combination.

[b] Excluding outliers and other images that were not included when modelling the light curves.

[c] The median time between consecutive images rounded to the nearest second. Due to factors such as weather, the day–night cycle, guiding and focus corrections the cadence is only approximately uniform over short timescales.

[d] The RMS of the residuals from the best-fit model.

BAKOS ET AL.

Table 2. Summary of photometric observations HAT-P-62–HAT-P-64

Instrument/Field[a]	Date(s)	# Images[b]	Cadence[c] (sec)	Filter	Precision[d] (mmag)
HAT-P-62					
HAT-5/G093	2012 Sep–2013 Apr	9472	213	r	15.1
HAT-7/G093	2012 Sep	240	213	r	13.7
HAT-8/G093	2012 Jul–2013 Apr	11093	217	r	12.9
FLWO 1.2 m/KeplerCam	2014 Dec 01	192	41	z	2.1
FLWO 1.2 m/KeplerCam	2014 Dec 09	376	41	i	1.7
FLWO 1.2 m/KeplerCam	2015 Jan 10	136	40	i	2.1
FLWO 1.2 m/KeplerCam	2015 Mar 04	363	39	i	3.5
FLWO 1.2 m/KeplerCam	2015 Sep 26	335	41	i	2.1
HAT-P-63					
HAT-5/G384	2009 May–2009 Jun	389	416	r	12.4
HAT-9/G384	2009 May–2009 Sep	2361	356	r	9.6
FLWO 1.2 m/KeplerCam	2013 Mar 13	111	86	i	2.1
FLWO 1.2 m/KeplerCam	2013 Mar 30	68	175	i	1.5
FLWO 1.2 m/KeplerCam	2013 Apr 16	157	86	i	2.4
HAT-P-64					
HAT-6/G357	2009 Sep–2010 Mar	3885	343	r	14.1
HAT-8/G357	2009 Sep–2010 Mar	9097	224	r	14.6
FLWO 1.2 m/KeplerCam	2011 Feb 02	93	105	i	1.5
FLWO 1.2 m/KeplerCam	2011 Oct 12	182	73	i	2.3
TESS/Sector 5	2018 Nov 15–2018 Dec 11	1149	1799	T	0.99

[a] For HATNet data we list the HATNet unit and field name from which the observations are taken. HAT-5, -6, -7 and -10 are located at Fred Lawrence Whipple Observatory in Arizona. HAT-8 and -9 are located on the roof of the Smithsonian Astrophysical Observatory Submillimeter Array hangar building at Mauna Kea Observatory in Hawaii. Each field corresponds to one of 838 fixed pointings used to cover the full 4π celestial sphere. All data from a given HATNet field are reduced together, while detrending through External Parameter Decorrelation (EPD) is done independently for each unique unit+field combination.

[b] Excluding outliers and other images that were not included when modelling the light curves.

[c] The median time between consecutive images rounded to the nearest second. Due to factors such as weather, the day–night cycle, guiding and focus corrections the cadence is only approximately uniform over short timescales.

[d] The RMS of the residuals from the best-fit model.

Figure 3. Generalized Lomb-Scargle periodogram of the HATNet observations of HAT-P-61 showing the possible detection of a $P = 10.6$ day periodic signal in the light curve of this star.

The HDS observations of HAT-P-63 were reduced to relative RVs following Sato et al. (2002, 2012) and to BSs following Torres et al. (2007). The RVs are seen to vary in phase with the photometric ephemeris of the TEP, and are consistent with the variations seen with the TRES and SOPHIE spectrographs for this system.

The ARCES spectrum of HAT-P-63 was reduced following Hartman et al. (2015) and Buchhave et al. (2012) and was used for reconnaissance. The RV and atmospheric parameters of HAT-P-63 determined from this spectrum are consistent with the results from TRES.

The FIES spectra of HAT-P-63 and HAT-P-64 were reduced following Buchhave et al. (2010). For HAT-P-63 the first spectrum was obtained using the medium resolution fiber, while the other spectra were obtained with the high resolution fiber. For HAT-P-64 all four spectra were obtained with the high resolution fiber. While the spectra were intended to be used for measuring the masses of the planetary companions, the resulting RV precision was insufficient for this purpose, given the small number of observations obtained. We therefore do not include these measurements in our analyses of HAT-P-63 or HAT-P-64.

NRES spectra of HAT-P-60 were collected from the McDonalds Observatory and Wise Observatory LCOGT 1 m facilities. We obtained 22 useful spectra with an SNR between 32 and 65, measured at ∼5150 Å. The exposure time for all spectra was 1800 sec. In order to obtain the wavelength calibrated spectra, we adapted the CERES pipeline (Brahm et al. 2017). We limited the order extraction to the central 50 orders, covering the wavelength range from 4194 Å to 7445 Å.

2.3. Ground-based photometric follow-up observations

In order to determine the physical parameters of each TEP system, we conducted follow-up photometric time-series observations of each object using KeplerCam on the 1.2 m telescope at FLWO. These observations are summarized in Tables 1 and 2, where we list the dates of the observed transit events, the number of images collected for each event, the cadence of the observations, the filters used, and the per-point photometric precision achieved. The images were reduced to light curves following Bakos et al. (2010), which are plotted in Figures 1–10. The data are provided in Table 5.

2.4. TESS Space-Based Photometry

Five of the seven planetary systems presented here were observed by the NASA *TESS* mission (Ricker et al. 2015), as summarized in Tables 1 and 2. Of particular note is HAT-P-59 which is located in the northern *TESS* continuous viewing zone, and had data from Sectors 14, 15, 16, 17, 18, 20 and 21 that we included in the analysis. We were not able to extract useful photometry for this system from the Sector 19 observations. The two systems that did not have *TESS* observations were either too close to the ecliptic plane (HAT-P-63), or located only on the edge of a CCD in Sector 19, with no useful data collected (HAT-P-62).

We note that HAT-P-59b and HAT-P-60b have both been independently identified as candidate transiting planets based on the *TESS* observations. HAT-P-59b (a.k.a. TOI-1826.01) is listed as a community-identified candidate on ExoFOP-TESS, while HAT-P-60b (a.k.a. TOI-1580.01) is listed as a candidate identified by the MIT quick-look pipeline. All of the systems presented here were detected and confirmed as planets by the HATNet team prior to the launch of the *TESS* mission.

The five systems with *TESS* observations were all observed in long-cadence mode, and we extracted simple aperture photometry for them from the *TESS* Full-Frame Image (FFI) data using the Lightkurve tool (Lightkurve Collaboration et al. 2018). Here we made use of the TESSCut API (Brasseur et al. 2019) to download 10×10 pixel FFI cutouts around each source, and made use of the automated mask routine in Lightkurve to generate the apertures using a threshold of 3.0, and to generate the background regions using a threshold of 0.001. We then used VARTOOLS (Hartman & Bakos 2016) to apply a moving median filter to remove large systematic variations from the light curves. This was done by first manually removing regions from the light curves with excessive systematic behavior, then masking the transits and performing a median filter with a 0.5 day window. We then performed a monotonic spline interpolation over the masked regions of the light curves to estimate the systematic corrections to apply to the in-transit portions of the data. Note that the proce-

BAKOS ET AL.

Table 3. Summary of spectroscopic observations

Instrument	UT Date(s)	# Spec.	Res. $(\lambda/\Delta\lambda)/1000$	S/N Range[a]	$\gamma_{\rm RV}$[b] $({\rm km\,s^{-1}})$	RV Precision[c] $({\rm m\,s^{-1}})$
HAT-P-58						
FLWO 1.5 m/TRES	2014 Jan 14–16	2	44	16–19	−35.96	97
Keck-I/HIRES+I$_2$	2014 Aug–Sep	7	55	35–115	$\cdots$	8.2
Keck-I/HIRES	2014 Aug 25	1	55	166	$\cdots$	$\cdots$
HAT-P-59						
FLWO 1.5 m/TRES	2013 Oct–Nov	13	44	13–25	−20.35	27
OHP 1.93 m/SOPHIE	2013 Oct–Nov	10	39	$\cdots$	−21.16	20
HAT-P-60						
FLWO 1.5 m/TRES	2013 Feb–Oct	13	44	20–61	6.58	17
OHP 1.93 m/SOPHIE	2013 Oct–Nov	8	39	$\cdots$	6.03	14
Keck-I/HIRES+I$_2$	2013 Dec–2016 Jan	8	55	140–196	$\cdots$	12
Keck-I/HIRES	2015 Nov 29	1	55	306	$\cdots$	$\cdots$
LCO 1m+ELP/NRES	2019 Dec-2020 Jan	12	53	32–65	5.92	63
LCO 1m+TLV/NRES	2019 Dec-2020 Jan	10	53	32–65	5.84	57
HAT-P-61						
FLWO 1.5 m/TRES	2014 Sep–Nov	18	44	12–22	4.81	53
Keck-I/HIRES+I$_2$	2015 Nov 27–29	3	55	63–95	$\cdots$	9.3
Keck-I/HIRES	2015 Nov 29	1	55	119	$\cdots$	$\cdots$
HAT-P-62						
FLWO 1.5 m/TRES	2014 Jan–Nov	15	44	15–25	50.42	37
HAT-P-63						
FLWO 1.5 m/TRES [d]	2012 Apr 6–28	3	44	13–15	−68.92	33
APO 3.5 m/ARCES	2012 Apr 30	1	31.5	18	−69.57	500
Subaru 8 m/HDS	2012 Sep 19	4	60	41–44	$\cdots$	$\cdots$
Subaru 8 m/HDS+I$_2$	2012 Sep 20–22	12	60	37–55	$\cdots$	4.7
NOT 2.5 m/FIES	2013 May 14	1	46	50	−69.11	100
NOT 2.5 m/FIES	2013 May 15–17	2	67	15–24	−69.045	66
OHP 1.93 m/SOPHIE	2013 Jun 3–13	7	39	$\cdots$	−69.60	23
HAT-P-64						
FLWO 1.5 m/TRES	2010 Oct–2011 Jan	2	44	25–28	25.220	58
NOT 2.5 m/FIES	2011 Oct 9–25	4	67	44–54	25.142	65
Keck-I/HIRES	2011 Jan–Sep	2	55	96–138	$\cdots$	$\cdots$
Keck-I/HIRES+I$_2$	2011 Jan–2012 Jan	7	55	80–113	$\cdots$	22
OHP 1.93 m/SOPHIE	2011 Dec 5–12	6	39	$\cdots$	24.49	35

[a] S/N per resolution element near 5180 Å. This was not reported for the OHP 1.93 m/SOPHIE observations.

[b] For high-precision RV observations included in the orbit determination this is the zero-point RV from the best-fit orbit. For other instruments it is the mean value. We do not provide this quantity for the Keck-I/HIRES observations, from which we have only measured relative RVs.

[c] For high-precision RV observations included in the orbit determination this is the scatter in the RV residuals from the best-fit orbit (which may include astrophysical jitter), for other instruments this is either an estimate of the precision (not including jitter), or the measured standard deviation. We do not provide this quantity for the I$_2$-free templates obtained with Keck-I/HIRES or Subaru/HDS.

[d] One of the TRES spectra of HAT-P-63 was low S/N and did not permit high precision RVs, so only two of the TRES RVs of this object are included in the analysis.

dures above will likely erase the rotation induced and other long-term variation of the stars. The resulting light curves are shown, together with the best-fit models, in Figures 2–14. These data are also made available in Table 5.

As for the HATNet observations, we used the VAR-TOOLS package to search the residual *TESS* light curves of each target for additional periodic transit signals using BLS, and for additional sinusoidal periodic signals using GLS. Table 4 gives the ephemeris information and significance for the top peak in the BLS spectrum of the *TESS* residuals for each system. None of the systems show strong evidence for additional periodic transit signals. In a few cases (HAT-P-58 and HAT-P-59) there is marginal evidence for signals with signal-to-pink noise ratio S/N> 7 (see Hartman & Bakos 2016 for a definition of this measure as used in VARTOOLS), though these are likely false alarms, and future observations by *TESS* in its extended mission should confirm or refute these. None of the systems shows evidence for a continuous periodic variation detected by GLS, though any such variations would likely be removed by the median-filtering procedure that we applied to the light curves.

2.5. *Speckle imaging observations*

In order to detect nearby stellar companions which may be diluting the transit signals, we obtained high spatial resolution speckle imaging observations of all seven systems. For HAT-P-58–HAT-P-62 and HAT-P-64 we used the Differential Speckle Survey Instrument (DSSI; Horch et al. 2009; Howell et al. 2011; Horch et al. 2011, 2012), while for HAT-P-63 we used the newer NN-explore Exoplanet Stellar Speckle Imager (NESSI; Scott et al. 2018). Both instruments were used with the WIYN 3.5 m telescope[2] at Kitt Peak National Observatory in Arizona.

The DSSI observations were gathered between the nights of UT 26 September 2015 and UT 3 October 2015. A dichroic beamsplitter is used to obtain simultaneous imaging through 692 nm and 880 nm filters. Each observation consists of a sequence of 1000 40 ms exposures read-out on 128×128 pixel ($2\rlap{.}''8 \times 2\rlap{.}''8$) subframes, which are reduced to reconstructed images following Horch et al. (2011). These images are searched for companions, and when none are detected, 5σ lower limits on the differential magnitude between a putative companion and the primary star are determined as a function of angular separation as described in Horch et al. (2011).

The NESSI observation was gathered on the night of UT 7 September 2017, in this case using a dichroic beamsplitter to image at 562 nm and 832 nm. The observing mode and reduction method are similar to those used for DSSI, and have been detailed in Scott et al. (2018). In this case the 256×256 pixel subframe has a field of view of $4\rlap{.}''6 \times 4\rlap{.}''6$.

For HAT-P-60 we obtained a single observation, while for the other six objects we obtained five observations apiece. In all cases no companions are detected within $1\rlap{.}''2$, and we place limits on the differential magnitudes in the blue and red filters as shown in Figures 4–20. We find limiting magnitude differences at $\sim 0\rlap{.}''2$ of

- **HAT-P-58** - $\Delta m_{692} > 3.22$ and $\Delta m_{880} > 2.65$
- **HAT-P-59** - $\Delta m_{692} > 3.14$ and $\Delta m_{880} > 2.74$
- **HAT-P-60** - $\Delta m_{692} > 4.04$ and $\Delta m_{880} > 3.41$
- **HAT-P-61** - $\Delta m_{692} > 2.85$ and $\Delta m_{880} > 2.62$
- **HAT-P-62** - $\Delta m_{692} > 3.16$ and $\Delta m_{880} > 2.81$
- **HAT-P-63** - $\Delta m_{562} > 3.82$ and $\Delta m_{832} > 3.55$
- **HAT-P-64** - $\Delta m_{692} > 2.60$ and $\Delta m_{880} > 2.80$

In addition to the companion limits based on the WIYN 3.5 m/DSSI observations, we also queried the UCAC 4 catalog (Zacharias et al. 2013) for neighbors within $20''$ and the Gaia DR2 catalog (Gaia Collaboration et al. 2018) for neighbors within $10''$ that may dilute either the HATNet or KeplerCam photometry. We find that HAT-P-60, HAT-P-62, and HAT-P-64 have fainter neighbors in Gaia DR2, while only the neighbor for HAT-P-62 is also detected in UCAC 4. The neighbors have separations and G-band magnitude differences as follows:

- **HAT-P-60** - $9\rlap{.}''088$ southeast, $\Delta G = 10.79$ mag
- **HAT-P-62** - $5\rlap{.}''565$ northwest, $\Delta G = 2.10$ mag, $\Delta V = 2.18$ mag
- **HAT-P-64** - $2\rlap{.}''510$ northwest, $\Delta G = 6.38$ mag

Based on the Gaia DR2 parallaxes the neighbors to HAT-P-60 and HAT-P-62 are background objects that are not physically associated with the planet hosts. No parallax, proper motion, or color information is available for the neighbor to HAT-P-64. This neighbor is at a projected separation of 1667 AU from the planet host, if it is physically associated. The neighbors to HAT-P-60 and HAT-P-64 are too faint to significantly affect the photometry and the resulting planet and stellar parameters, and can be ruled out as the source of the detected

---

[2] The WIYN Observatory is a joint facility of the University of Wisconsin-Madison, Indiana University, the National Optical Astronomy Observatory and the University of Missouri.

Table 4. BLS search for additional transits in the residual *TESS* light curves

System	Period	T_C	duration	depth	N_{transits}	S/N[a]
	(d)	$(\text{BJD}_{TDB} - 245000)$	(hr)	(mmag)		
HAT-P-58	22.130[b]	8829.949	20.5	1.4	1	7.75
HAT-P-59	19.956	8702.753	10.1	0.48	8	7.66
HAT-P-60	6.7248	8799.080	6.9	0.45	4	6.84
HAT-P-61	17.447	8816.517	8.3	1.4	2	6.75
HAT-P-64	0.2151	8438.105	0.072	1.4	17	5.80

[a] The signal-to-pink-noise ratio as calculated by VARTOOLS (Hartman & Bakos 2016).

[b] In this case only a single transit event is identified by BLS, and the period is not meaningful.
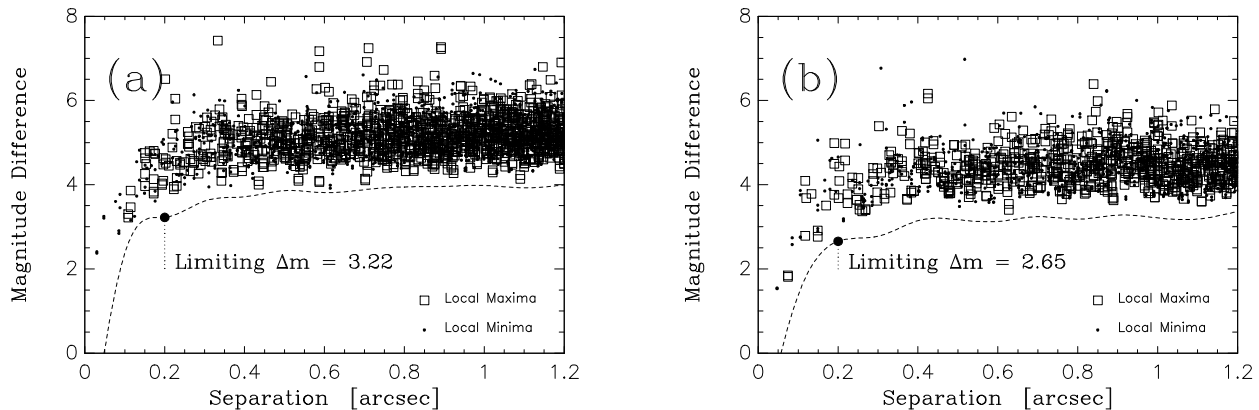
Figure 4. Limits on the relative magnitude of a resolved companion to HAT-P-58 as a function of angular separation based on speckle imaging observations from WIYN 3.5 m/DSSI. The left panel shows the limits for the 692 nm filter, the right shows limits for the 880 nm filter.

transit signals. We do account for the neighbor to HAT-P-62 ($\Delta G = 2.10$ mag) in the analysis of this system as described in Section 3.3.

3. ANALYSIS

We analyzed the photometric and spectroscopic observations of HAT-P-58–HAT-P-64 to determine the parameters of each system. The analysis followed the methods discussed in detail most recently by Hartman et al. (2019). Here we give a brief summary of the procedure.

3.1. *Properties of the parent star*

High-precision atmospheric parameters, including the effective surface temperature $T_{\text{eff}\star}$, the surface gravity $\log g$, the metallicity [Fe/H], and the projected rotational velocity $v \sin i$, were determined by applying SPC to our high resolution spectra. For HAT-P-58 through HAT-P-63 this analysis was performed on the TRES

spectra, while for HAT-P-64 we made use of the Keck-I/HIRES I_2-free template spectra. The analysis is performed seperately on each spectrum and we take the weighted average of the results over all spectra obtained for each target. Here we assume minimum uncertainties of 50 K on $T_{\text{eff}\star}$, 0.10 dex on $\log g$, 0.08 dex on [Fe/H], and 0.5 km s^{-1} on $v \sin i$, which reflects the systematic uncertainty in the method, and is based on applying the SPC analysis to observations of spectroscopic standard stars. Following Torres et al. (2012), we then revised the atmospheric parameters of the stars in an iterative fashion. We carried out a joint analysis of the light curves and RV curves to determine the mean stellar density $\rho_\star$ for each host. We then combined the $T_{\text{eff}\star}$ and [Fe/H] from the spectra with $\rho_\star$ to determine the surface gravities via interpolation within the Yonsei-Yale theoretical stellar isochrones (Y2; Yi et al. 2001). The surface gravities were then fixed to the values from this procedure in a second iteration of SPC where only $T_{\text{eff}\star}$, [Fe/H] and

Table 5. Light curve data for HAT-P-58–HAT-P-63.

Object[a]	BJD$_{TDB}$[b] (2,400,000+)	Mag[c]	σ_{Mag}	Mag(orig)[d]	Filter	Instrument
HAT-P-58	56239.13511	0.00565	0.01008	⋯	r	HATNet
HAT-P-58	56235.12147	−0.01055	0.01209	⋯	r	HATNet
HAT-P-58	56207.02456	−0.00900	0.01093	⋯	r	HATNet
HAT-P-58	56243.14926	−0.00973	0.01036	⋯	r	HATNet
HAT-P-58	56194.98348	0.03111	0.01042	⋯	r	HATNet
HAT-P-58	56211.03898	−0.00313	0.01037	⋯	r	HATNet
HAT-P-58	56194.98363	−0.00382	0.00963	⋯	r	HATNet
HAT-P-58	56375.60748	−0.02041	0.01786	⋯	r	HATNet
HAT-P-58	56198.99820	−0.02555	0.01558	⋯	r	HATNet
HAT-P-58	56383.63531	0.01115	0.01428	⋯	r	HATNet

[a] Either HAT-P-58, HAT-P-59, HAT-P-60, HAT-P-61, HAT-P-62, HAT-P-63 or HAT-P-64.

[b] Barycentric Julian Date on the dynamical time system, including the correction for leap seconds.

[c] The out-of-transit level has been subtracted. For observations made with the HATNet instruments (identifed by "HN" in the "Instrument" column) these magnitudes have been corrected for trends using the EPD and TFA procedures applied either *prior* to fitting the transit model, or in conjunction with fitting a box-shaped transit. This procedure, together with blending for nearby stars, may lead to an artificial dilution in the transit depths. The blend factors for the HATNet light curves are listed in Tables 10 and 11. For observations made with follow-up instruments (anything other than "HN" in the "Instrument" column), the magnitudes have been corrected for a quadratic trend in time, for variations correlated with three PSF shape parameters, and for trends correlated with variations seen in the light curves of other stars in the field (the TFA method) fit simultaneously with the transit.

[d] Raw magnitude values without correction for the quadratic trend in time, for trends correlated with the shape of the PSF, or application of TFA. These are only reported for the follow-up observations.

Note— This table is available in a machine-readable form in the online journal. A portion is shown here for guidance regarding its form and content.

$v \sin i$ were allowed to vary. Note that this procedure for determining the fixed value of $\log g_\star$ was performed prior to the release of Gaia DR2, and we choose not to perform an additional iteration of SPC making use of the Gaia DR2 parallax. The expected change in the atmospheric parameters are in all cases smaller than the systematic uncertainties.

The final spectroscopic parameters, together with catalog astrometry and photometry are listed for the host stars in Tables 6 and 7.

The final atmospheric parameters are then treated as observations which are simultaneously fitted, together with the light curves, RV curves, parallaxes, and catalog broad-band photometry as described in Section 3.3.

Here the fitting procedure makes use of the PARSEC stellar evolution models (Marigo et al. 2017) to constrain the physical properties of the stars. The final derived physical parameters of the stars, based on this method, including $M_\star$, $R_\star$, $\log g_\star$, $\rho_\star$, $L_\star$, $T_{\mathrm{eff}\star}$, [Fe/H], the age of the system, the V-band extinction A$_V$, and the distance to the system are listed in Tables 8 and 9. Note that the values of $T_{\mathrm{eff}\star}$ and [Fe/H] listed here are the optimized values that are varied in the joint analysis, and may differ from the values for these parameter determined from modeling the spectra listed in Tables 6 and 7. Figures 1–10 show the de-reddened Gaia DR2 $BP - RP$ colors vs. absolute G magnitudes for each star compared to the PARSEC stellar evolution models, and also show

the broad-band spectral energy distribution of each star compared to the PARSEC models.

3.2. *Excluding blend scenarios*

In order to exclude blend scenarios we carried out an analysis following Hartman et al. (2012), as updated in Hartman et al. (2019). Here we attempt to model the available photometric data (including light curves and catalog broad-band photometric measurements) for each object as a blend between an eclipsing binary star system and a third star along the line of sight (either a physical association, or a chance alignment). The physical properties of the stars are constrained using the Padova isochrones (Girardi et al. 2002), while we also require that the brightest of the three stars in the blend have atmospheric parameters consistent with those measured with SPC. We also simulate composite cross-correlation functions (CCFs) and use them to predict RVs and BSs for each blend scenario considered.

Based on this analysis we rule out blended stellar eclipsing binary scenarios for all seven systems. The results for each object are as follows:

- *HAT-P-58*: All blend models tested yield higher χ^2 fits to the photometry than the model of a single star with a transiting planet, and can be rejected with $\sim 1\sigma$ confidence. Those models which cannot be rejected with at least 5σ confidence based solely on the photometry predict BS variations in excess of $1\,\mathrm{km\,s^{-1}}$ (however, the measured BS r.m.s. scatter from HIRES is $21\,\mathrm{m\,s^{-1}}$).

- *HAT-P-59*: All blend models tested yield higher χ^2 fits to the photometry than the model of a single star with a transiting planet, and can be rejected with 3σ confidence. Those models which cannot be rejected with at least 5σ confidence based solely on the photometry predict BS variations in excess of $100\,\mathrm{m\,s^{-1}}$ (however, the measured BS r.m.s. scatter from TRES is $50\,\mathrm{m\,s^{-1}}$) and RV variations that do not reproduce the observed sinusoidal variation.

- *HAT-P-60*: All blend models tested can be rejected with at least 5σ confidence based solely on the photometry.

- *HAT-P-61*: Similar to HAT-P-59, all blend models tested yield higher χ^2 fits to the photometry than the model of a single star with a transiting planet, and can be rejected with 2σ confidence based on the photometry alone. Those models which cannot be rejected with at least 5σ confidence based solely on the photometry predict HIRES BS variations in excess of $100\,\mathrm{m\,s^{-1}}$ (the measured BS r.m.s. scatter from HIRES is $5\,\mathrm{m\,s^{-1}}$), TRES BS variations in excess of $200\,\mathrm{m\,s^{-1}}$ (the measured BS r.m.s. scatter from TRES is $50\,\mathrm{m\,s^{-1}}$) and RV variations that do not reproduce the observed sinusoidal variation.

- *HAT-P-62*: All blend models tested have higher χ^2 fits to the photometry than the model of a single star with a transiting planet, and can be rejected with at least 1σ confidence. Those models which cannot be rejected with at least 5σ confidence can be rejected based on the BS observations. These blend models yield an r.m.s. scatter for the BSs in excess of $390\,\mathrm{m\,s^{-1}}$, whereas the measured TRES BS r.m.s. scatter is $35\,\mathrm{m\,s^{-1}}$.

- *HAT-P-63*: Similar to HAT-P-59, all blend models tested yield higher χ^2 fits to the photometry than the model of a single star with a transiting planet, and can be rejected with 1.5σ confidence based on the photometry alone. Those models which cannot be rejected with at least 5σ confidence based solely on the photometry predict HDS BS variations in excess of $60\,\mathrm{m\,s^{-1}}$ (the measured BS r.m.s. scatter from HDS is $13\,\mathrm{m\,s^{-1}}$), SOPHIE BS variations in excess of $400\,\mathrm{m\,s^{-1}}$ (the measured BS r.m.s. scatter from SOPHIE is $26\,\mathrm{m\,s^{-1}}$) and RV variations in excess of $\sim 200\,\mathrm{m\,s^{-1}}$ that do not reproduce the observed sinusoidal variation.

- *HAT-P-64*: All blend models tested have higher χ^2 fits to the photometry than the model of a single star with a transiting planet, and can be rejected with at least 1σ confidence. Those models which cannot be rejected with at least 5σ confidence predict a BS r.m.s. scatter of at least $160\,\mathrm{m\,s^{-1}}$, compared to the measured BS r.m.s. of $35\,\mathrm{m\,s^{-1}}$ for the Keck/HIRES observations.

The analysis described above was carried out before the release of Gaia DR2 or *TESS* data. The consistency between the distance inferred for each source by this method, assuming it is a single star with a planet, and the Gaia DR2 distance only bolsters the basic conclusion that none of these systems is a blended stellar eclipsing binary. Moreover, the *TESS* light curves showed no features (such as secondary eclipses or large ellipsoidal variations) that would be indicative of a blended eclipsing binary that might motivate a re-analysis.

3.3. *Global modeling of the data*

In order to determine the physical parameters of the TEP systems, we carried out a global modeling of the

Table 6. Astrometric, Spectroscopic and Photometric parameters for HAT-P-58, HAT-P-59, HAT-P-60 and HAT-P-61

Parameter	HAT-P-58 Value	HAT-P-59 Value	HAT-P-60 Value	HAT-P-61 Value	Source
Astrometric properties and cross-identifications					
TIC-ID	9443323	229400092	354469661	259506033	
TOI-ID	$\cdots$	1826.01	1580.01	$\cdots$	
2MASS-ID	04352318+5652055	19295008+6231452	01530777+5203140	05015525+5007526	
GSC-ID	GSC 3740-01482	GSC 4234-02195	GSC 3292-01330	GSC 3352-00595	
GAIA DR2-ID	277493615044741376	2241743203599727744	359678187913760384	256580182331399296	
R.A. (J2000)	$04^h35^m23.1828s$	$19^h29^m50.0701s$	$01^h53^m07.7727s$	$05^h01^m55.2577s$	GAIA DR2
Dec. (J2000)	$+56°52'05.5848''$	$+62°31'45.1751''$	$+52°03'14.01977''$	$+50°07'52.5746''$	GAIA DR2
$\mu_{\mathrm{R.A.}}$ (mas yr^{-1})	-10.883 ± 0.072	20.957 ± 0.046	26.51 ± 0.11	-11.021 ± 0.067	GAIA DR2
$\mu_{\mathrm{Dec.}}$ (mas yr^{-1})	11.862 ± 0.064	-6.056 ± 0.043	6.165 ± 0.075	-21.440 ± 0.063	GAIA DR2
parallax (mas)	1.912 ± 0.047	3.738 ± 0.019	4.260 ± 0.049	2.923 ± 0.035	GAIA DR2
Spectroscopic properties					
$T_{\mathrm{eff}\star}$ (K)	5931 ± 50	5665 ± 50	6462 ± 50	5551 ± 50	SPC[a]
[Fe/H]	0.012 ± 0.080	0.409 ± 0.080	-0.237 ± 0.080	0.396 ± 0.080	SPC
$v \sin i$ (km s^{-1})	4.91 ± 0.50	3.04 ± 0.50	10.42 ± 0.50	3.69 ± 0.50	SPC
v_{mac} (km s^{-1})	1.0	1.0	1.0	1.0	Assumed
v_{mic} (km s^{-1})	2.0	2.0	2.0	2.0	Assumed
γ_{RV} (m s^{-1})	-35.97 ± 0.10	-20.477 ± 0.027	6.582 ± 0.027	4.810 ± 0.022	TRES[b]
S_{HK}	0.150 ± 0.010	$\cdots$	0.1236 ± 0.0022	0.240 ± 0.012	HIRES
$\log R'_{\mathrm{HK}}$	-5.057 ± 0.072	$\cdots$	-5.309 ± 0.033	-4.719 ± 0.032	HIRES
Photometric properties					
G (mag)[c]	12.72020 ± 0.00020	11.67870 ± 0.00030	9.56360 ± 0.00030	12.93860 ± 0.00040	GAIA DR2
BP (mag)[c]	13.1422 ± 0.0016	12.0587 ± 0.0011	9.8631 ± 0.0012	13.4067 ± 0.0018	GAIA DR2
RP (mag)[c]	12.13470 ± 0.00090	11.15850 ± 0.00050	9.1320 ± 0.0013	12.33560 ± 0.00080	GAIA DR2
B (mag)	13.690 ± 0.089	12.581 ± 0.094	10.230 ± 0.040	14.040 ± 0.056	APASS[d]
V (mag)	12.971 ± 0.073	11.883 ± 0.065	9.710 ± 0.050	13.188 ± 0.029	APASS[d]
I (mag)	$\cdots$	11.073 ± 0.078	9.077 ± 0.042	12.05 ± 0.12	TASS Mark IV[e]
g (mag)	13.28 ± 0.12	12.16 ± 0.10	$\cdots$	13.550 ± 0.045	APASS[d]
r (mag)	12.74 ± 0.12	11.650 ± 0.050	$\cdots$	12.915 ± 0.033	APASS[d]
i (mag)	12.50 ± 0.12	11.478 ± 0.050	9.421 ± 0.040	12.675 ± 0.051	APASS[d]
J (mag)	11.429 ± 0.022	10.581 ± 0.020	8.677 ± 0.052	11.598 ± 0.021	2MASS
H (mag)	11.075 ± 0.020	10.268 ± 0.018	8.396 ± 0.029	11.263 ± 0.029	2MASS
K_s (mag)	10.978 ± 0.023	10.208 ± 0.022	8.368 ± 0.031	11.141 ± 0.020	2MASS

[a] SPC = Stellar Parameter Classification procedure for the analysis of high-resolution spectra (Buchhave et al. 2012), applied to the TRES spectra of HAT-P-58–HAT-P-61. These parameters rely primarily on SPC, but have a small dependence also on the iterative analysis incorporating the isochrone search and global modeling of the data.

[b] In addition to the uncertainty listed here, there is a ~ 0.1 km s^{-1} systematic uncertainty in transforming the velocities to the IAU standard system.

[c] The listed uncertainties for the Gaia DR2 photometry are taken from the catalog. For the analysis we assume additional systematic uncertainties of 0.002 mag, 0.005 mag and 0.003 mag for the G, BP and RP bands, respectively.

[d] From APASS DR6 for as listed in the UCAC 4 catalog (Zacharias et al. 2013).

[e] From the Amateur Sky Survey (TASS) catalog release IV (Droege et al. 2006).

Table 7. Astrometric, Spectroscopic and Photometric parameters for HAT-P-62, HAT-P-63 and HAT-P-64

Parameter	HAT-P-62 Value	HAT-P-63 Value	HAT-P-64 Value	Source
Astrometric properties and cross-identifications				
TIC-ID	453064665	1635721458	455036659	
TOI-ID	$\cdots$	$\cdots$	$\cdots$	
2MASS-ID	04580102+4818038	17581730+0545409	04355384+0225526	
GSC-ID	GSC 3348-01101	GSC 0429-01697	GSC 0086-00341	
GAIA DR2-ID	255397142179844224	4474644332250439552	3279418602369232000	
R.A. (J2000)	$04^h58^m01.0287s$	$17^h58^m17.3121s$	$04^h35^m53.8469s$	GAIA DR2
Dec. (J2000)	$+48°18'03.7570''$	$+05°45'40.9400''$	$+02°25'52.6434''$	GAIA DR2
$\mu_{R.A.}$ (mas yr^{-1})	14.732 ± 0.080	-14.871 ± 0.036	7.784 ± 0.079	GAIA DR2
$\mu_{Dec.}$ (mas yr^{-1})	-43.776 ± 0.061	-0.301 ± 0.039	-3.863 ± 0.044	GAIA DR2
parallax (mas)	2.839 ± 0.040	2.450 ± 0.024	1.505 ± 0.035	GAIA DR2
Spectroscopic properties				
$T_{eff\star}$ (K)	5601 ± 50	5365 ± 50	6302 ± 50	SPC[a]
[Fe/H]	0.449 ± 0.080	0.428 ± 0.080	-0.010 ± 0.080	SPC
$v \sin i$ (km s^{-1})	3.55 ± 0.50	3.22 ± 0.50	12.70 ± 0.50	SPC
v_{mac} (km s^{-1})	1.0	1.0	1.0	Assumed
v_{mic} (km s^{-1})	2.0	2.0	2.0	Assumed
γ_{RV} (m s^{-1})	50.424 ± 0.025	-68.994 ± 0.057	25.22 ± 0.10	FEROS or HARPS[b]
S_{HK}	$\cdots$	$\cdots$	0.1453 ± 0.0068	HIRES
$\log R'_{HK}$	$\cdots$	$\cdots$	-5.062 ± 0.057	HIRES
Photometric properties				
G (mag)[c]	12.43620 ± 0.00030	13.51060 ± 0.00030	12.62210 ± 0.00010	Gaia DR2
BP (mag)[c]	12.8932 ± 0.0013	14.0381 ± 0.0012	12.98580 ± 0.00080	Gaia DR2
RP (mag)[c]	11.84000 ± 0.00090	12.84760 ± 0.00080	12.09530 ± 0.00070	Gaia DR2
B (mag)	$\cdots$	14.729 ± 0.066	13.446 ± 0.011	APASS[d]
V (mag)	$\cdots$	13.753 ± 0.065	12.771 ± 0.010	APASS[d]
I (mag)	$\cdots$	$\cdots$	12.105 ± 0.070	TASS Mark IV[e]
g (mag)	$\cdots$	14.258 ± 0.026	13.062 ± 0.013	APASS[d]
r (mag)	$\cdots$	13.418 ± 0.093	12.553 ± 0.075	APASS[d]
i (mag)	$\cdots$	13.136 ± 0.086	12.440 ± 0.037	APASS[d]
J (mag)	11.144 ± 0.029	12.021 ± 0.021	11.485 ± 0.026	2MASS
H (mag)	10.803 ± 0.041	11.630 ± 0.028	11.225 ± 0.025	2MASS
K_s (mag)	10.701 ± 0.026	11.512 ± 0.023	11.123 ± 0.021	2MASS

[a] SPC = Stellar Parameter Classification procedure for the analysis of high-resolution spectra (Buchhave et al. 2012), applied to the TRES spectra of HAT-P-62 and HAT-P-63, and to the HIRES I$_2$-free template spectra of HAT-P-64. These parameters rely primarily on SPC, but have a small dependence also on the iterative analysis incorporating the isochrone search and global modeling of the data.

[b] In addition to the uncertainty listed here, there is a ~ 0.1 km s^{-1} systematic uncertainty in transforming the velocities to the IAU standard system.

[c] The listed uncertainties for the Gaia DR2 photometry are taken from the catalog. For the analysis we assume additional systematic uncertainties of 0.002 mag, 0.005 mag and 0.003 mag for the G, BP and RP bands, respectively.

[d] From APASS DR6 for as listed in the UCAC 4 catalog (Zacharias et al. 2013).

[e] From the Amateur Sky Survey (TASS) catalog release IV (Droege et al. 2006).

Table 8. Derived stellar parameters for HAT-P-58, HAT-P-59, HAT-P-60 and HAT-P-61

Parameter	HAT-P-58 Value	HAT-P-59 Value	HAT-P-60 Value	HAT-P-61 Value
$M_\star$ ($M_\odot$)	1.031 ± 0.028	1.008 ± 0.022	1.435 ± 0.012	1.004 ± 0.033
$R_\star$ ($R_\odot$)	1.530 ± 0.034	1.1038 ± 0.0073	$2.197^{+0.027}_{-0.020}$	0.938 ± 0.011
$\log g_\star$ (cgs)	4.082 ± 0.020	4.356 ± 0.013	3.9114 ± 0.0097	4.496 ± 0.021
$\rho_\star$ (g cm^{-3})	0.405 ± 0.026	1.059 ± 0.038	$0.1909^{+0.0054}_{-0.0071}$	1.715 ± 0.094
$L_\star$ ($L_\odot$)	2.86 ± 0.15	1.132 ± 0.015	6.44 ± 0.17	0.767 ± 0.031
$T_{\mathrm{eff}\star}$ (K)	6078 ± 48	5678 ± 16	6212 ± 26	5587 ± 45
[Fe/H]	-0.224 ± 0.057	0.217 ± 0.049	0.037 ± 0.037	0.194 ± 0.060
Age (Gyr)	$7.11^{+0.27}_{-0.72}$	7.3 ± 1.0	$2.765^{+0.042}_{-0.056}$	2.6 ± 2.0
A_V (mag)	0.737 ± 0.034	0.048 ± 0.011	0.120 ± 0.019	0.389 ± 0.043
Distance (pc)	519 ± 11	267.3 ± 1.3	235.4 ± 2.3	343.2 ± 3.9

NOTE— The listed parameters are those determined through the joint differential evolution Markov Chain analysis described in Section 3.3. For all four systems the fixed-circular-orbit model has a higher Bayesian evidence than the eccentric-orbit model. We therefore assume a fixed circular orbit in generating the parameters listed here.

Table 9. Derived stellar parameters for HAT-P-62, HAT-P-63 and HAT-P-64

Parameter	HAT-P-62 Value	HAT-P-63 Value	HAT-P-64 Value
$M_\star$ ($M_\odot$)	1.023 ± 0.020	0.925 ± 0.023	1.298 ± 0.021
$R_\star$ ($R_\odot$)	1.170 ± 0.016	$0.9661^{+0.0110}_{-0.0082}$	$1.735^{+0.041}_{-0.028}$
$\log g_\star$ (cgs)	4.312 ± 0.015	4.435 ± 0.015	4.072 ± 0.015
$\rho_\star$ (g cm^{-3})	0.901 ± 0.042	1.448 ± 0.061	0.350 ± 0.018
$L_\star$ ($L_\odot$)	1.232 ± 0.053	0.714 ± 0.028	$4.66^{+0.29}_{-0.17}$
$T_{\mathrm{eff}\star}$ (K)	5629 ± 48	5400^{+55}_{-39}	6457 ± 29
[Fe/H]	0.414 ± 0.090	0.251 ± 0.061	$-0.113^{+0.027}_{-0.056}$
Age (Gyr)	8.1 ± 1.1	9.0 ± 1.7	2.88 ± 0.13
A_V (mag)	0.339 ± 0.046	0.506 ± 0.046	$0.650^{+0.014}_{-0.021}$
Distance (pc)	353.1 ± 4.4	408.0 ± 4.0	655^{+17}_{-11}

NOTE— The listed parameters are those determined through the joint differential evolution Markov Chain analysis described in Section 3.3. For all three systems the fixed-circular-orbit model has a higher Bayesian evidence than the eccentric-orbit model. We therefore assume a fixed circular orbit in generating the parameters listed here.

HATNet, KeplerCam, and *TESS* photometry, the high-precision RV measurements, the SPC $T_{\mathrm{eff}\star}$ and [Fe/H] measurements, the Gaia DR2 parallax, and the Gaia DR2, APASS, TASS Mark IV, 2MASS and WISE broad-band photometry (G, BP, RP, B, V, g, r, i, R, I_C, J, H, K_S, W_1, W_2, W_3, W_4; where available).

We fit Mandel & Agol (2002) transit models to the light curves assuming quadratic limb darkening. The limb darkening coefficients are allowed to vary in the fit, but we use the tabulations from Claret et al. (2012,

2013) and Claret (2018) to place informative Gaussian prior constraints on their values, assuming a prior uncertainty of 0.2 for each coefficient.

We allow for a dilution of the HATNet transit depth in cases where there are neighbors blended with the targets in the low spatial resolution survey images (HAT-P-61–HAT-P-64). For *TESS* we allowed for dilution for all five observed systems, and also binned the model to account for the 30 min exposure time (Kipping 2010). For the KeplerCam light curves we include a quadratic trend in

time, linear trends with up to three parameters describing the shape of the PSF, and a simultaneous application of the Trend Filtering Algorithm (Kovács et al. 2005) in our model for each event to correct for systematic errors in the photometry. For HAT-P-62 we also include dilution factors in the KeplerCam model to account for the blending with the 5″21 neighbor. To do this we simulate KeplerCam images of the primary target and its neighbor using the observed PSF and drawing i-band magnitudes for each component from Normal distributions with means and standard deviations based on the measured i magnitudes for each source from APASS. We also simulate images without the neighbor. We then carry out aperture photometry on the simulated images and compare the flux measured with and without the neighbor to determine the expected dilution. The median and standard deviation of the dilution are then calculated from all simulations for a given night to establish Gaussian priors which are placed on the dilution parameters which we vary in our modeling.

We fit Keplerian orbits to the RV curves allowing the zero-point for each instrument to vary independently in the fit, and allowing for RV jitter which we also vary as a free parameter for each instrument.

To model the additional stellar atmospheric, parallax and photometry observations we introduce four new model parameters which are allowed to vary in the fit: the distance modulus $(m - M)_0$, the V-band extinction A_V, and the stellar atmospheric parameters $T_{\rm eff\star}$ and [Fe/H]. Each link in the Markov Chain yields a combination of ($T_{\rm eff\star}$, $\rho_\star$, [Fe/H]) which we use to determine the stellar mass, radius, $\log g$, luminosity, and absolute magnitude in various bandpasses by comparison with the PARSEC stellar evolution models (specifically PARSEC realease v1.2S + CLIBRI release PR16, as in Marigo et al. 2017) which we generated using the CMD 3.0 web interface by L. Girardi[3]. Note that $\rho_\star$ is not varied directly in the fit, but rather can be computed

from the other transit and orbital parameters which are varied. These absolute magnitudes, together with the model distance modulus and polynomial relations for the extinction in each bandpass as a function of A_V and $T_{\rm eff\star}$ are used to compute model values for the broad-band photometry measurements to be compared to the observations. Here we assume systematic errors of 0.002 mag, 0.005 mag and 0.003 mag on the G, BP and RP photometry, respectively, following Evans et al. (2018). These systematic uncertainties are added in quadrature to the statistical uncertainties on the measurements listed in the Gaia DR2 catalog.

For A_V we made use of the MWDUST 3D Galactic extinction model (Bovy et al. 2016) to tabulate the extinction in 0.1 kpc steps in the direction of the source. For a given $(m - M)_0$ we then perform linear interpolation among these values to estimate the expected A_V at that distance. We treat this expected value as a Gaussian prior, with a 1σ uncertainty of 20% the maximum value.

We used a Differential Evolution Markov Chain Monte Carlo procedure to explore the fitness landscape and to determine the posterior distribution of the parameters. When a proposed link in the Markov Chain falls outside of the parameter values spanned by the stellar evolution models (e.g., if a star with a density greater than what is allowed by the stellar evolution models at a given temperature and metallicity is proposed) the link is rejected and the previous link is retained. In this manner the fitting procedure used here forces the solutions to match to the theoretical stellar evolution models. We tried fitting both fixed-circular-orbits and free-eccentricity models to the data, and for all seven systems find that the data are consistent with a circular orbit. We therefore adopt the parameters that come from the fixed-circular-orbit models for all of the systems. The resulting parameters for HAT-P-58b, HAT-P-59b, HAT-P-60b, and HAT-P-61b are listed in Table 10, while for HAT-P-62b, HAT-P-63b and HAT-P-64b they are listed in Table 11.

Table 10. Orbital and planetary parameters for HAT-P-58b, HAT-P-59b, HAT-P-60b and HAT-P-61b

Parameter	HAT-P-58b Value	HAT-P-59b Value	HAT-P-60b Value	HAT-P-61b Value
Light curve parameters				
P (days)	4.0138379 ± 0.0000024	4.1419771 ± 0.0000012	4.7947813 ± 0.0000024	$1.90231289 \pm 0.00000077$

Table 10 *continued*

[3] http://stev.oapd.inaf.it/cgi-bin/cmd

Table 10 *(continued)*

Parameter	HAT-P-58b Value	HAT-P-59b Value	HAT-P-60b Value	HAT-P-61b Value
T_c (BJD$_{\mathrm{TDB}}$ − 2450000) [a] ...	7369.03094 ± 0.00056	8618.54088 ± 0.00021	8360.94029 ± 0.00056	7851.21119 ± 0.00047
T_{14} (days) [a]	0.1729 ± 0.0015	0.09747 ± 0.00097	0.2098 ± 0.0015	0.0691 ± 0.0012
$T_{12} = T_{34}$ (days) [a]	0.0193 ± 0.0010	0.02624 ± 0.00099	0.02557 ± 0.00073	0.01372 ± 0.00085
$a/R_\star$	7.02 ± 0.15	9.87 ± 0.12	$6.146^{+0.057}_{-0.077}$	6.90 ± 0.13
$\zeta/R_\star$ [b]	13.00 ± 0.10	26.81 ± 0.41	10.81 ± 0.10	35.46 ± 0.88
$R_p/R_\star$	0.0895 ± 0.0017	0.10452 ± 0.00096	0.07622 ± 0.00055	0.0984 ± 0.0025
b^2	$0.285^{+0.033}_{-0.032}$	$0.689^{+0.013}_{-0.015}$	$0.446^{+0.014}_{-0.018}$	$0.589^{+0.024}_{-0.026}$
$b \equiv a\cos i/R_\star$	$0.534^{+0.030}_{-0.031}$	$0.8299^{+0.0077}_{-0.0089}$	$0.668^{+0.011}_{-0.014}$	$0.767^{+0.015}_{-0.017}$
i (deg)	85.64 ± 0.34	85.180 ± 0.100	83.75 ± 0.17	83.62 ± 0.24
HATNet blend factors [c]				
Blend factor 1	$\cdots$	$\cdots$	$\cdots$	0.87 ± 0.10
Blend factor 2	$\cdots$	$\cdots$	$\cdots$	0.915 ± 0.065
TESS blend factors [c]				
Blend factor 1	0.940 ± 0.038	0.997 ± 0.012	0.9957 ± 0.0018	0.694 ± 0.040
Blend factor 2	$\cdots$	0.9993 ± 0.0018	$\cdots$	$\cdots$
Blend factor 3	$\cdots$	0.9982 ± 0.0047	$\cdots$	$\cdots$
Blend factor 4	$\cdots$	0.9989 ± 0.0038	$\cdots$	$\cdots$
Blend factor 5	$\cdots$	0.996 ± 0.023	$\cdots$	$\cdots$
Blend factor 6	$\cdots$	0.996 ± 0.012	$\cdots$	$\cdots$
Blend factor 7	$\cdots$	0.9993 ± 0.0018	$\cdots$	$\cdots$
Limb-darkening coefficients [d]				
c_1, R	$\cdots$	$\cdots$	$\cdots$	0.38 ± 0.16
c_2, R	$\cdots$	$\cdots$	$\cdots$	0.36 ± 0.17
c_1, r	0.23 ± 0.14	0.43 ± 0.16	0.47 ± 0.15	0.40 ± 0.16
c_2, r	0.25 ± 0.17	0.36 ± 0.17	0.28 ± 0.15	0.39 ± 0.16
c_1, i	0.18 ± 0.10	0.32 ± 0.14	0.18 ± 0.12	0.32 ± 0.16
c_2, i	0.14 ± 0.15	0.21 ± 0.15	0.09 ± 0.14	0.30 ± 0.16
c_1, z	$\cdots$	$\cdots$	$0.137^{+0.129}_{-0.096}$	$\cdots$
c_2, z	$\cdots$	$\cdots$	0.12 ± 0.15	$\cdots$
c_1, T	0.26 ± 0.13	0.16 ± 0.11	0.19 ± 0.11	0.31 ± 0.14
c_2, T	0.24 ± 0.16	0.29 ± 0.14	0.23 ± 0.15	0.29 ± 0.16
RV parameters				
K (m s^{-1})	46.4 ± 3.6	192.6 ± 7.7	54.1 ± 3.5	173 ± 11
e [e]	< 0.073	< 0.030	< 0.250	< 0.113
RV jitter HIRES (m s^{-1}) [f] ...	< 12.6	$\cdots$	12.3 ± 3.7	< 61.3
RV jitter TRES (m s^{-1})	$\cdots$	< 38.4	< 12.4	39 ± 11
RV jitter SOPHIE (m s^{-1}) ...	$\cdots$	< 17.6	< 15.0	$\cdots$
RV jitter NRES/ELP (m s^{-1})	$\cdots$	$\cdots$	56 ± 13	$\cdots$
RV jitter NRES/TLV (m s^{-1})	$\cdots$	$\cdots$	22 ± 19	$\cdots$
Planetary parameters				
M_p (M_{J})	0.372 ± 0.030	1.540 ± 0.067	0.574 ± 0.038	1.057 ± 0.070
R_p (R_{J})	1.332 ± 0.043	1.123 ± 0.013	1.631 ± 0.024	0.899 ± 0.027
$C(M_p, R_p)$ [g]	0.02	-0.16	-0.02	-0.04

Table 10 *continued*

Table 10 *(continued)*

Parameter	HAT-P-58b Value	HAT-P-59b Value	HAT-P-60b Value	HAT-P-61b Value
ρ_p (g cm^{-3})	0.194 ± 0.024	1.347 ± 0.081	0.164 ± 0.013	1.80 ± 0.20
$\log g_p$ (cgs)	2.714 ± 0.045	3.481 ± 0.023	2.730 ± 0.032	3.510 ± 0.040
a (AU)	0.04994 ± 0.00044	0.05064 ± 0.00037	0.06277 ± 0.00017	0.03010 ± 0.00034
$T_{\rm eq}$ (K)	1622 ± 18	1277.8 ± 6.5	1772 ± 12	1505 ± 16
Θ [h]	0.0269 ± 0.0023	0.1367 ± 0.0058	0.0306 ± 0.0020	0.0702 ± 0.0047
$\log_{10}\langle F \rangle$ (cgs) [i]	9.193 ± 0.019	8.7787 ± 0.0088	9.347 ± 0.012	9.063 ± 0.018

[a] Times are in Barycentric Julian Date on the dynamical time system, including the correction for leap seconds. T_c: Reference epoch of mid transit that minimizes the correlation with the orbital period. T_{14}: total transit duration, time between first to last contact; $T_{12} = T_{34}$: ingress/egress time, time between first and second, or third and fourth contact.

Note— For all four systems the fixed-circular-orbit model has a higher Bayesian evidence than the eccentric-orbit model. We therefore assume a fixed circular orbit in generating the parameters listed here.

[b] Reciprocal of the half duration of the transit used as a jump parameter in our MCMC analysis in place of $a/R_\star$. It is related to $a/R_\star$ by the expression $\zeta/R_\star = a/R_\star (2\pi(1 + e\sin\omega))/(P\sqrt{1-b^2}\sqrt{1-e^2})$ (Bakos et al. 2010).

[c] Scaling factor applied to the model transit that is fit to the HATNet and *TESS* light curves. This factor accounts for dilution of the transit due to blending from neighboring stars and over-filtering of the light curve (in cases where we do not apply signal-reconstruction TFA). These factors are varied in the fit, and we allow independent factors for observations obtained for different HATNet fields and different *TESS* sectors. For HAT-P-58–HAT-P-60 we do not include these factors for HATNet because the stars are well isolated on the HATNet images, and we applied signal-reconstruction TFA to preserve the signal shape while filtering the light curves.

[d] Values for a quadratic law. These are allowed to vary in the fit, using the tabulations from Claret et al. (2012, 2013) and Claret (2018) to place informative Gaussian prior constraints on their values.

[e] The 95% confidence upper limit on the eccentricity determined when $\sqrt{e}\cos\omega$ and $\sqrt{e}\sin\omega$ are allowed to vary in the fit.

[f] Term added in quadrature to the formal RV uncertainties for each instrument. This is treated as a free parameter in the fitting routine. In cases where the jitter is consistent with zero we list the 95% confidence upper limit.

[g] Correlation coefficient between the planetary mass M_p and radius R_p estimated from the posterior parameter distribution.

[h] The Safronov number is given by $\Theta = \frac{1}{2}(V_{\rm esc}/V_{\rm orb})^2 = (a/R_p)(M_p/M_\star)$ (see Hansen & Barman 2007).

[i] Incoming flux per unit surface area, averaged over the orbit.

Table 11. Orbital and planetary parameters for HAT-P-62b, HAT-P-63b and HAT-P-64b

Parameter	HAT-P-62b Value	HAT-P-63b Value	HAT-P-64b Value
Light curve parameters			
P (days)	2.6453235 ± 0.0000039	3.377728 ± 0.000013	4.0072320 ± 0.0000017
T_c (BJD$_{\rm TDB}$ − 2450000) [a] ..	7118.38979 ± 0.00044	6382.94256 ± 0.00053	7751.46354 ± 0.00063
T_{14} (days) [a]	0.1293 ± 0.0012	0.1222 ± 0.0016	0.2052 ± 0.0020
$T_{12} = T_{34}$ (days) [a]	0.01183 ± 0.00050	0.01392 ± 0.00058	0.0199 ± 0.0010
$a/R_\star$	6.93 ± 0.11	9.56 ± 0.14	6.67 ± 0.12
$\zeta/R_\star$ [b]	17.02 ± 0.17	18.45 ± 0.27	10.79 ± 0.11
$R_p/R_\star$	0.0942 ± 0.0019	0.1191 ± 0.0032	0.1007 ± 0.0034
b^2	$0.063^{+0.036}_{-0.035}$	$0.069^{+0.040}_{-0.030}$	$0.054^{+0.046}_{-0.030}$
$b \equiv a\cos i/R_\star$	$0.250^{+0.064}_{-0.084}$	$0.262^{+0.068}_{-0.066}$	$0.232^{+0.085}_{-0.079}$
i (deg)	87.93 ± 0.64	88.45 ± 0.44	88.01 ± 0.70

Table 11 *continued*

Table 11 *(continued)*

Parameter	HAT-P-62b Value	HAT-P-63b Value	HAT-P-64b Value
HATNet blend factors [c]			
Blend factor	0.839 ± 0.055	$\cdots$	0.748 ± 0.072
TESS blend factors [c]			
Blend factor	$\cdots$	$\cdots$	0.871 ± 0.062
Limb-darkening coefficients [d]			
c_1, r	0.36 ± 0.15	0.44 ± 0.15	0.26 ± 0.14
c_2, r	0.31 ± 0.18	0.38 ± 0.16	0.26 ± 0.17
c_1, i	0.33 ± 0.10	0.47 ± 0.13	0.26 ± 0.14
c_2, i	0.22 ± 0.16	0.41 ± 0.14	0.27 ± 0.17
c_1, T	$\cdots$	$\cdots$	0.29 ± 0.11
c_2, T	$\cdots$	$\cdots$	0.37 ± 0.16
RV parameters			
K (m s^{-1})	110 ± 13	87.3 ± 3.2	62 ± 18
e [e]	< 0.101	< 0.069	< 0.101
RV jitter HIRES (m s^{-1}) [f] ..	$\cdots$	$\cdots$	21 ± 10
RV jitter TRES (m s^{-1})	33 ± 11	< 1.9	$\cdots$
RV jitter SOPHIE (m s^{-1}) ..	$\cdots$	16 ± 10	< 69.2
RV jitter HDS (m s^{-1})	$\cdots$	< 2.4	$\cdots$
Planetary parameters			
M_p ($M_{\rm J}$)	0.761 ± 0.088	0.614 ± 0.024	$0.58^{+0.18}_{-0.13}$
R_p ($R_{\rm J}$)	1.073 ± 0.029	1.119 ± 0.033	1.703 ± 0.070
$C(M_p, R_p)$ [g]	0.02	-0.25	0.06
ρ_p (g cm^{-3})	0.77 ± 0.11	0.540 ± 0.055	$0.144^{+0.046}_{-0.035}$
$\log g_p$ (cgs)	3.214 ± 0.056	3.082 ± 0.034	2.69 ± 0.12
a (AU)	0.03772 ± 0.00024	0.04294 ± 0.00035	0.05387 ± 0.00030
$T_{\rm eq}$ (K)	1512 ± 13	1237 ± 11	1766^{+22}_{-16}
Θ [h]	0.0522 ± 0.0061	0.0506 ± 0.0026	$0.0281^{+0.0084}_{-0.0064}$
$\log_{10}\langle F \rangle$ (cgs) [i]	9.072 ± 0.015	8.722 ± 0.015	$9.341^{+0.021}_{-0.016}$

NOTE— For all three systems the fixed-circular-orbit model has a higher Bayesian evidence than the eccentric-orbit model. We therefore assume a fixed circular orbit in generating the parameters listed here. For all further tablenotes please refer to Table. 10.

4. DISCUSSION

We presented the discovery of seven hot Jupiters transiting bright stars. These planets were first identified as transiting planet candidates by the HATNet survey from among some 6 million stars that have been observed to date since 2004. They were subsequently confirmed and accurately characterized using high-precision time-series photometry from FLWO 1.2 m/KeplerCam, and the NASA *TESS* mission, and high-resolution spectroscopy, enabling high-precision radial velocity measurements, carried out with the FLWO 1.5 m/TRES, Keck-I/HIRES, OHP 1.93 m/SOPHIE, Subaru 8 m/HDS, APO 3.5 m/ARCES, NOT 2.5 m/FIES, and LCOGT 1 m/NRES telescopes/instruments.

The planets discovered here contribute to the growing sample of transiting planets with precisely measured masses and radii. All seven planets have radii measured to better than ∼10% precision, and six of them have masses measured to this level of precision as well. Such planets are valuable contributions to the growing sample of well-characterized exoplanets which may be used in statistical studies to test theories of planet formation and evolution. In fact, the planets presented here have already been included in one such study (Hartman et al. 2016).

Close-in giant planets transiting bright stars, such as these, can also be followed-up in a modest amount of time using current facilities to measure their orbital (mis-)alignments and probe the planetary atmospheres. We estimate that the amplitude of the Rossiter-McLaughlin effect is: $35\,\mathrm{m\,s^{-1}}$, $18\,\mathrm{m\,s^{-1}}$, $36\,\mathrm{m\,s^{-1}}$, $23\,\mathrm{m\,s^{-1}}$, $30\,\mathrm{m\,s^{-1}}$, $44\,\mathrm{m\,s^{-1}}$, and $128\,\mathrm{m\,s^{-1}}$, for HAT-P-58b–HAT-P-64b, respectively. Given the host star brightnesses, measured RV jitter values, and transit durations, the effect would be detectable using facilities ranging from FLWO 1.5 m/TRES (HAT-P-60b which orbits a $V = 9.710 \pm 0.050$ mag host star, and HAT-P-64b with its large amplitude signal and long-lasting transits), to Keck-I/HIRES (HAT-P-59b). With $a/R_\star > 9$, and $T_{\mathrm{eff}\star} < 6000\,\mathrm{K}$, HAT-P-59b and HAT-P-63b may be particularly interesting objects for which to observe this effect, in an effort to determine whether giant planets transiting cool stars become less well aligned as the strength of the tidal interaction with their host stars decreases (e.g., Albrecht et al. 2012).

As regards atmospheric characterization, with its 1% deep transits lasting almost five hours, and large atmospheric scale height ($\log g_p = 2.69 \pm 0.12$), HAT-P-64b is perhaps the most promising of the planets discovered here for having readily detectable features in its transmission spectrum. These may be atomic or molecular absorption features as seen, for example, in the spectrum of the inflated Neptune HAT-P-26b, (Wakeford et al. 2017), among many other planets. Alternatively, this may be evidence of an atmospheric haze revealed through Rayleigh-scattering, as seen, for example, in the spectrum of the highly inflated hot Jupiter HAT-P-32b, (Mallonn & Wakeford 2017), again among many planets. With a planetary radius of $1.703 \pm 0.070\,R_{\mathrm{J}}$, HAT-P-64b is also one of the largest known transiting exoplanets (as of 2018 July there are only 23 transiting planets listed in the NASA exoplanet archive with larger radii). The planet follows the well-established trend between high-equilibrium temperature and inflated radius (e.g., Fortney et al. 2007; Enoch et al. 2011; Kovács et al. 2010; Béky et al. 2011; Enoch et al. 2012).

Including the systems presented here, a total of 67 transiting planets have now been discovered and published by HATNet. In addition to these, some 17 planets discovered by other teams have been independently detected in HATNet light curves (KELT-1, KELT-3, Kepler-6, Kepler-12, KOI-13, Qatar-1, TrES-2, TrES-3, TrES-5, WASP-2, WASP-10, WASP-13, WASP-24, WASP-33, WASP-48, XO-3, and XO-5), and more than a dozen additional transiting planets have been detected by HATNet and confirmed through follow-up observations, but have not yet been published. Altogether at

least ~ 100 transiting exoplanets have been detected by HATNet, and certainly more planets remain to be discovered among the 500 remaining candidates that have not yet been confirmed or set aside as false positives or false alarms. The Hungarian-made Automated Telescope Network (HATNet) continues to operate in a fully autonomous manner, and will continue to produce high-precision high-cadence time-series photometry for millions of stars over a large swath of the Northern sky. Over the past 16 years it has amassed a rich database of light curves for six million stars.

The NASA *TESS* mission (Ricker et al. 2015) uses a set of four lenses, very similar in diameter to those used by HATNet, to survey the entire sky. Although the HATNet light curves are of lower photometric precision than *TESS*, the observations are made at higher spatial resolution than *TESS*, and are useful for identifying *TESS* candidates that are actually blended stellar eclipsing binary objects. The HATNet light curves may also be used in conjunction with the *TESS* data to search for longer period planets than could be found in the typical 27.4 d *TESS* observing windows alone.

The planet HAT-P-59b presented has made for a particularly fruitful synergy between HATNet and *TESS*. This planet lies 10°.4 from the northern ecliptic pole, and is thus within the Northern continuous viewing zone of *TESS*. It will be observed continuously for approximately 1 yr by *TESS*, and we have already included seven sectors of data in our analysis of this system.

We plan to continue operating HATNet for the foreseeable future, and anticipate widening the region of parameter space to which we are sensitive to planets (i.e., toward finding sub-Neptune-size planets and planets with periods of several tens of days), by combining HATNet and *TESS* data, and by extending the time coverage of regions on the sky previously observed by HATNet.

ACKNOWLEDGMENTS

REFERENCES

Albrecht, S., Winn, J. N., Johnson, J. A., et al. 2012, ApJ, 757, 18

Bakos, G., Noyes, R. W., Kovács, G., et al. 2004, PASP, 116, 266

Bakos, G. Á., Torres, G., Pál, A., et al. 2010, ApJ, 710, 1724

Bakos, G. Á., Csubry, Z., Penev, K., et al. 2013, PASP, 125, 154

Béky, B., Bakos, G. Á., Hartman, J., et al. 2011, ApJ, 734, 109

Bieryla, A., Hartman, J. D., Bakos, G. Á., et al. 2014, AJ, 147, 84

Boisse, I., Hartman, J. D., Bakos, G. Á., et al. 2013, A&A, 558, A86

Bouchy, F., Hébrard, G., Udry, S., et al. 2009, A&A, 505, 853

Bovy, J., Rix, H.-W., Green, G. M., Schlafly, E. F., & Finkbeiner, D. P. 2016, ApJ, 818, 130

Brahm, R., Jordán, A., & Espinoza, N. 2017, PASP, 129, 034002

Brasseur, C. E., Phillip, C., Fleming, S. W., Mullally, S. E., & White, R. L. 2019, Astrocut: Tools for creating cutouts of TESS images

Buchhave, L. A., Bakos, G. Á., Hartman, J. D., et al. 2010, ApJ, 720, 1118

Buchhave, L. A., Latham, D. W., Johansen, A., et al. 2012, Nature, 486, 375

Butler, R. P., Marcy, G. W., Williams, E., et al. 1996, PASP, 108, 500

Charbonneau, D., Brown, T. M., Noyes, R. W., & Gilliland, R. L. 2002, ApJ, 568, 377

Claret, A. 2018, A&A, 618, A20

Claret, A., Hauschildt, P. H., & Witte, S. 2012, A&A, 546, A14

—. 2013, A&A, 552, A16

Djupvik, A. A., & Andersen, J. 2010, in Highlights of Spanish Astrophysics V, ed. J. M. Diego, L. J. Goicoechea, J. I. González-Serrano, & J. Gorgas, 211

Droege, T. F., Richmond, M. W., Sallman, M. P., & Creager, R. P. 2006, PASP, 118, 1666

Enoch, B., Collier Cameron, A., & Horne, K. 2012, A&A, 540, A99

Enoch, B., Anderson, D. R., Barros, S. C. C., et al. 2011, AJ, 142, 86

Evans, D. W., Riello, M., De Angeli, F., et al. 2018, ArXiv e-prints, 1804.09368

Fűrész, G. 2008, PhD thesis, Univ. of Szeged, Hungary

Fortney, J. J., Marley, M. S., & Barnes, J. W. 2007, ApJ, 659, 1661

Gaia Collaboration, Brown, A. G. A., Vallenari, A., et al. 2018, ArXiv e-prints, 1804.09365

Girardi, L., Bertelli, G., Bressan, A., et al. 2002, A&A, 391, 195

Hansen, B. M. S., & Barman, T. 2007, ApJ, 671, 861

Hartman, J. D., & Bakos, G. Á. 2016, Astronomy and Computing, 17, 1

Hartman, J. D., Bakos, G. Á., Béky, B., et al. 2012, AJ, 144, 139

Hartman, J. D., Bhatti, W., Bakos, G. Á., et al. 2015, AJ, 150, 168

Hartman, J. D., Bakos, G. Á., Bhatti, W., et al. 2016, AJ, 152, 182

Hartman, J. D., Bakos, G. Á., Bayliss, D., et al. 2019, AJ, 157, 55

Horch, E. P., Bahi, L. A. P., Gaulin, J. R., et al. 2012, AJ, 143, 10

Horch, E. P., van Altena, W. F., Howell, S. B., Sherry, W. H., & Ciardi, D. R. 2011, AJ, 141, 180

Horch, E. P., Veillette, D. R., Baena Gallé, R., et al. 2009, AJ, 137, 5057

Howell, S. B., Everett, M. E., Sherry, W., Horch, E., & Ciardi, D. R. 2011, AJ, 142, 19

Isaacson, H., & Fischer, D. 2010, ApJ, 725, 875

Kambe, E., Sato, B., Takeda, Y., et al. 2002, PASJ, 54, 865

Kipping, D. M. 2010, MNRAS, 408, 1758

Kovács, G., Bakos, G., & Noyes, R. W. 2005, MNRAS, 356, 557

Kovács, G., Zucker, S., & Mazeh, T. 2002, A&A, 391, 369

Kovács, G., Bakos, G. Á., Hartman, J. D., et al. 2010, ApJ, 724, 866

Latham, D. W., Bakos, G. Á., Torres, G., et al. 2009, ApJ, 704, 1107

Lightkurve Collaboration, Cardoso, J. V. d. M., Hedges, C., et al. 2018, Lightkurve: Kepler and TESS time series analysis in Python, Astrophysics Source Code Library

Mallon, M., & Wakeford, H. R. 2017, ArXiv e-prints, 1707.08328

Mandel, K., & Agol, E. 2002, ApJL, 580, L171

Marigo, P., Girardi, L., Bressan, A., et al. 2017, ApJ, 835, 77

Noguchi, K., Aoki, W., Kawanomoto, S., et al. 2002, PASJ, 54, 855

Noyes, R. W., Hartmann, L. W., Baliunas, S. L., Duncan, D. K., & Vaughan, A. H. 1984, ApJ, 279, 763

Pál, A. 2012, MNRAS, 421, 1825

Pepper, J., Pogge, R. W., DePoy, D. L., et al. 2007, PASP, 119, 923

Pollacco, D. L., Skillen, I., Collier Cameron, A., et al. 2006, PASP, 118, 1407

Queloz, D., Eggenberger, A., Mayor, M., et al. 2000, A&A, 359, L13

Ricker, G. R., Winn, J. N., Vanderspek, R., et al. 2015, Journal of Astronomical Telescopes, Instruments, and Systems, 1, 014003

Sato, B., Kambe, E., Takeda, Y., Izumiura, H., & Ando, H. 2002, PASJ, 54, 873

Sato, B., Hartman, J. D., Bakos, G. Á., et al. 2012, PASJ, 64, 97

Scott, N. J., Howell, S. B., Horch, E. P., & Everett, M. E. 2018, PASP, 130, 054502

Siverd, R. J., Brown, T. M., Barnes, S., et al. 2018, in Ground-based and Airborne Instrumentation for Astronomy VII, ed. C. J. Evans, L. Simard, & H. Takami, Vol. 10702, International Society for Optics and Photonics (SPIE), 1918 – 1929

Torres, G., Fischer, D. A., Sozzetti, A., et al. 2012, ApJ, 757, 161

Torres, G., Bakos, G. Á., Kovács, G., et al. 2007, ApJL, 666, L121

Vogt, S. S., Allen, S. L., Bigelow, B. C., et al. 1994, in Society of Photo-Optical Instrumentation Engineers (SPIE) Conference Series, Vol. 2198, Society of Photo-Optical Instrumentation Engineers (SPIE) Conference Series, ed. D. L. Crawford & E. R. Craine, 362

Wakeford, H. R., Sing, D. K., Kataria, T., et al. 2017, Science, 356, 628

Wang, S.-i., Hildebrand, R. H., Hobbs, L. M., et al. 2003, in Society of Photo-Optical Instrumentation Engineers (SPIE) Conference Series, Vol. 4841, Instrument Design and Performance for Optical/Infrared Ground-based Telescopes, ed. M. Iye & A. F. M. Moorwood, 1145–1156

Yi, S., Demarque, P., Kim, Y.-C., et al. 2001, ApJS, 136, 417

Zacharias, N., Finch, C. T., Girard, T. M., et al. 2013, AJ, 145, 44

Zechmeister, M., & Kürster, M. 2009, A&A, 496, 577

Zhou, G., Huang, C. X., Bakos, G. Á., et al. 2019, AJ, 158, 141

HAT-P-59 P=4.14d M_P=1.54M_{Jup} R_P=1.12R_{Jup} M_S=1.01M_{Sun} R_S=1.10R_{Sun}
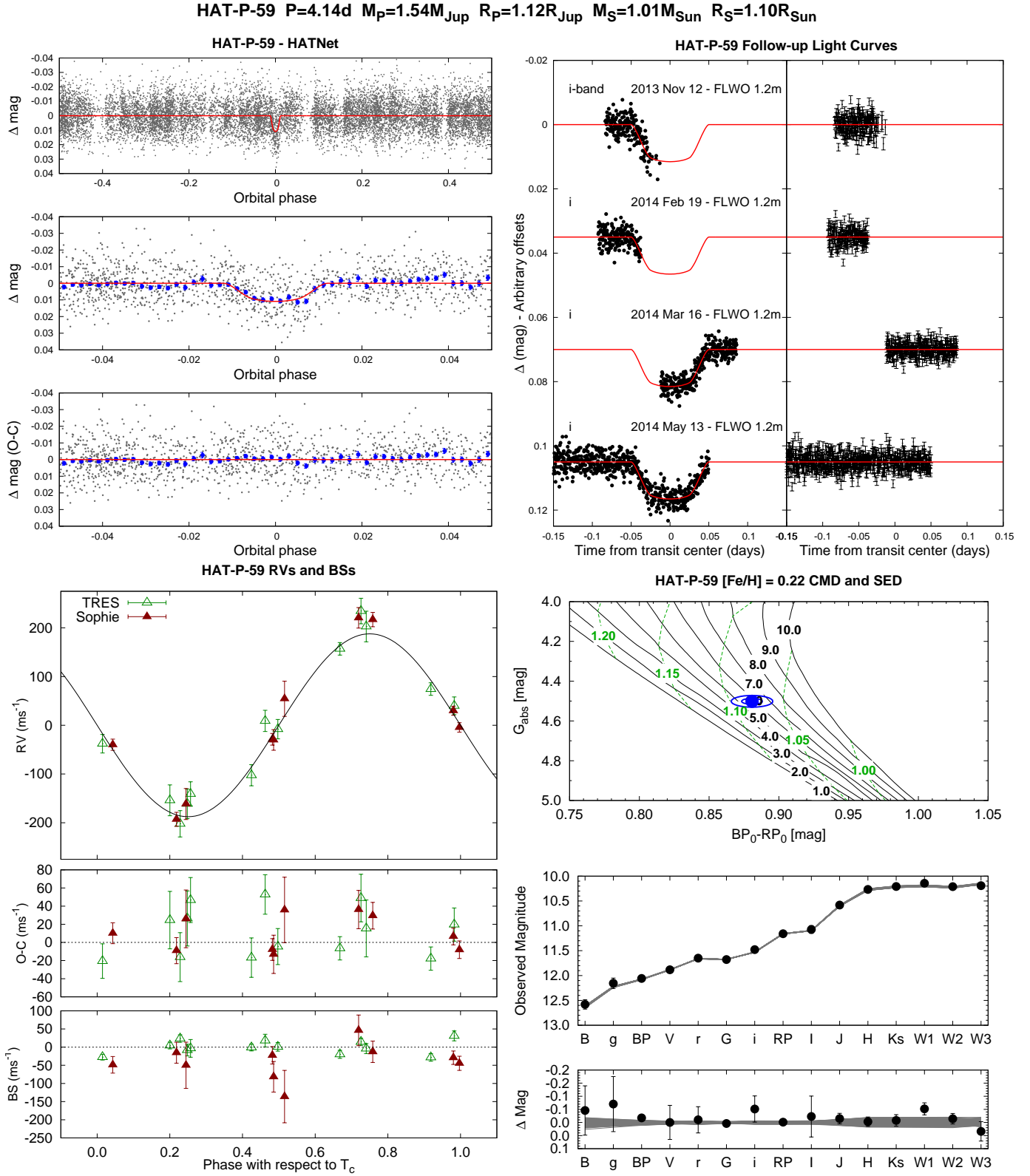
Figure 5. Observations of HAT-P-59 together with our best-fit model. Please refer to Figure 1 for a more detailed caption. The *TESS* light curve for this system is shown in Figure 11.
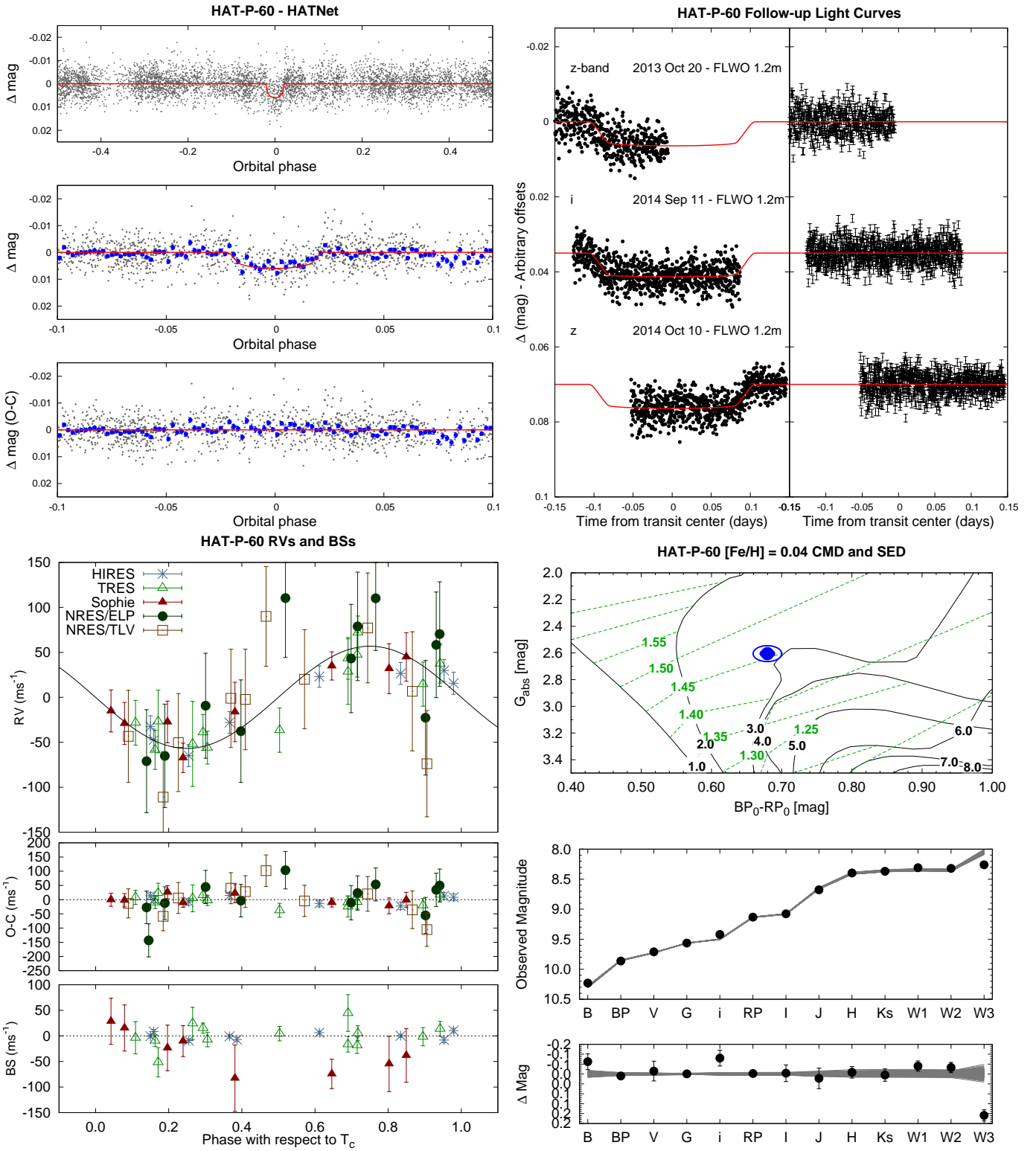
Figure 6. Observations of HAT-P-60 together with our best-fit model. Please refer to Figure 1 for a more detailed caption. The *TESS* light curve for this system is shown in Figure 12.

HAT-P-61 P=1.90d M$_P$=1.06M$_{Jup}$ R$_P$=0.90R$_{Jup}$ M$_S$=1.00M$_{Sun}$ R$_S$=0.94R$_{Sun}$

Figure 7. Observations of HAT-P-61 together with our best-fit model. Please refer to Figure 1 for a more detailed caption. The *TESS* light curve for this system is shown in Figure 13.

HAT-P-62 P=2.65d M_P=0.76M_Jup R_P=1.07R_Jup M_S=1.02M_Sun R_S=1.17R_Sun
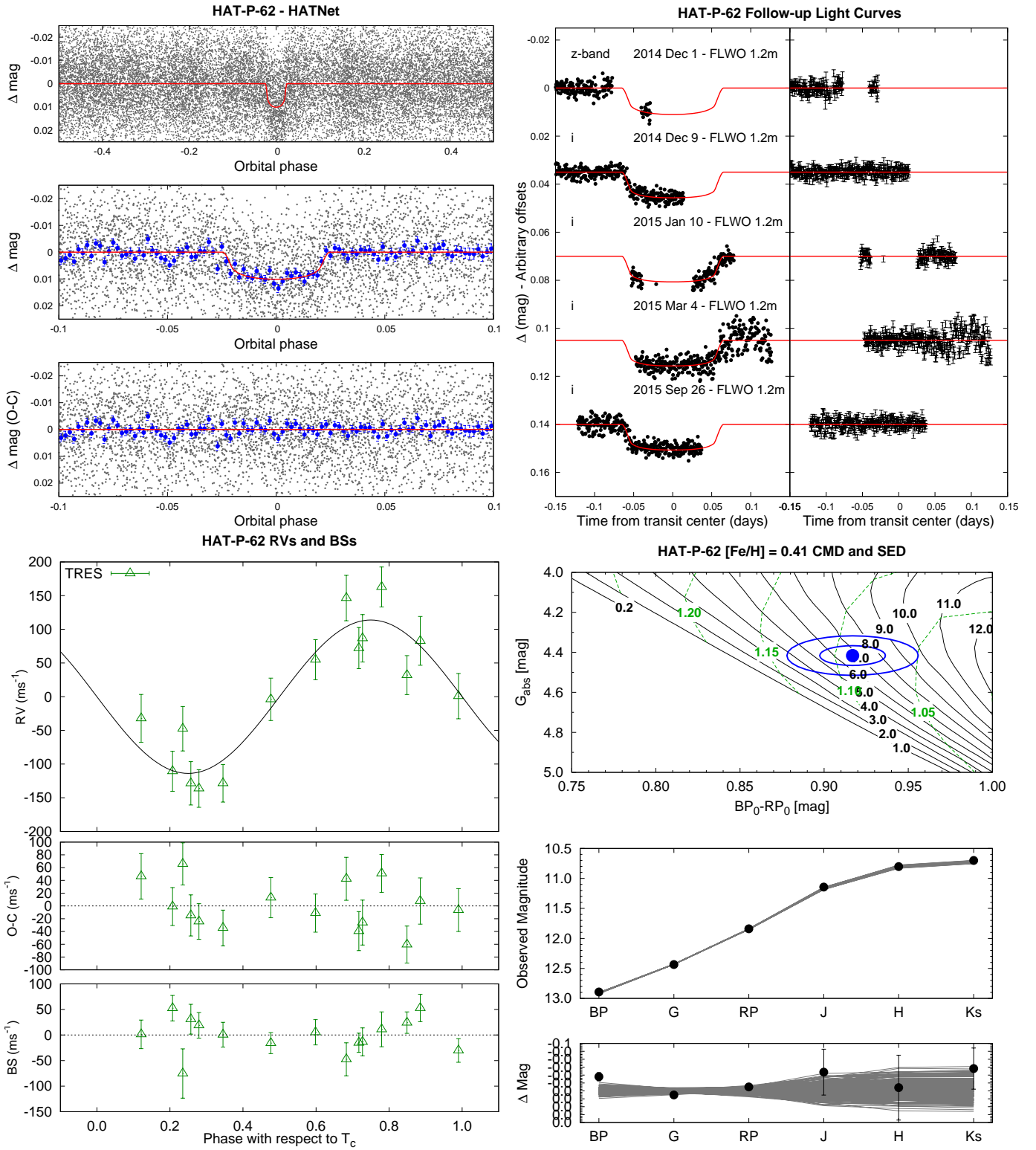
Figure 8. Observations of HAT-P-62 together with our best-fit model. Please refer to Figure 1 for a more detailed caption.

HAT-P-63 P=3.38d M$_P$=0.61M$_{Jup}$ R$_P$=1.12R$_{Jup}$ M$_S$=0.92M$_{Sun}$ R$_S$=0.97R$_{Sun}$
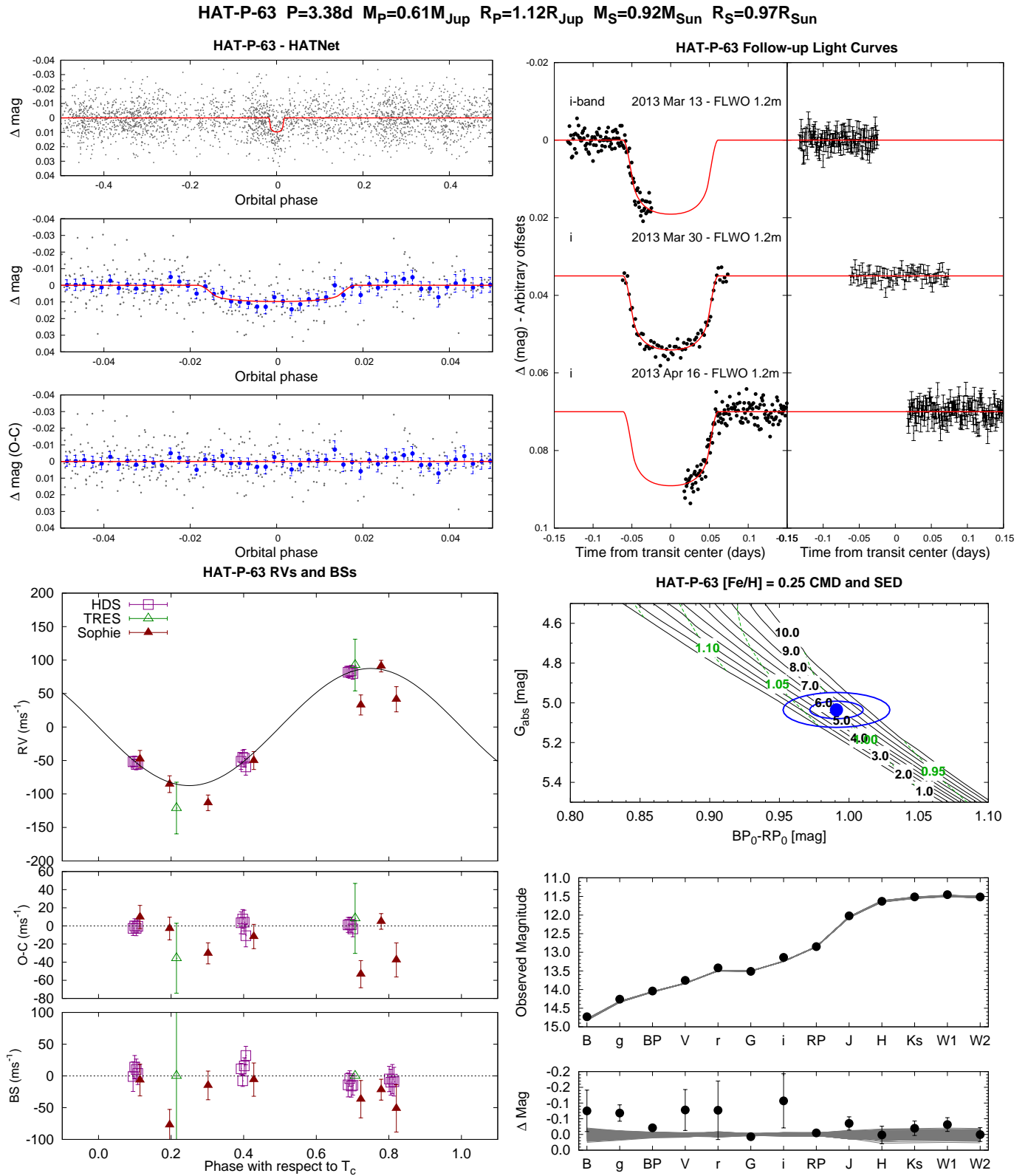
Figure 9. Observations of HAT-P-63 together with our best-fit model. Please refer to Figure 1 for a more detailed caption.

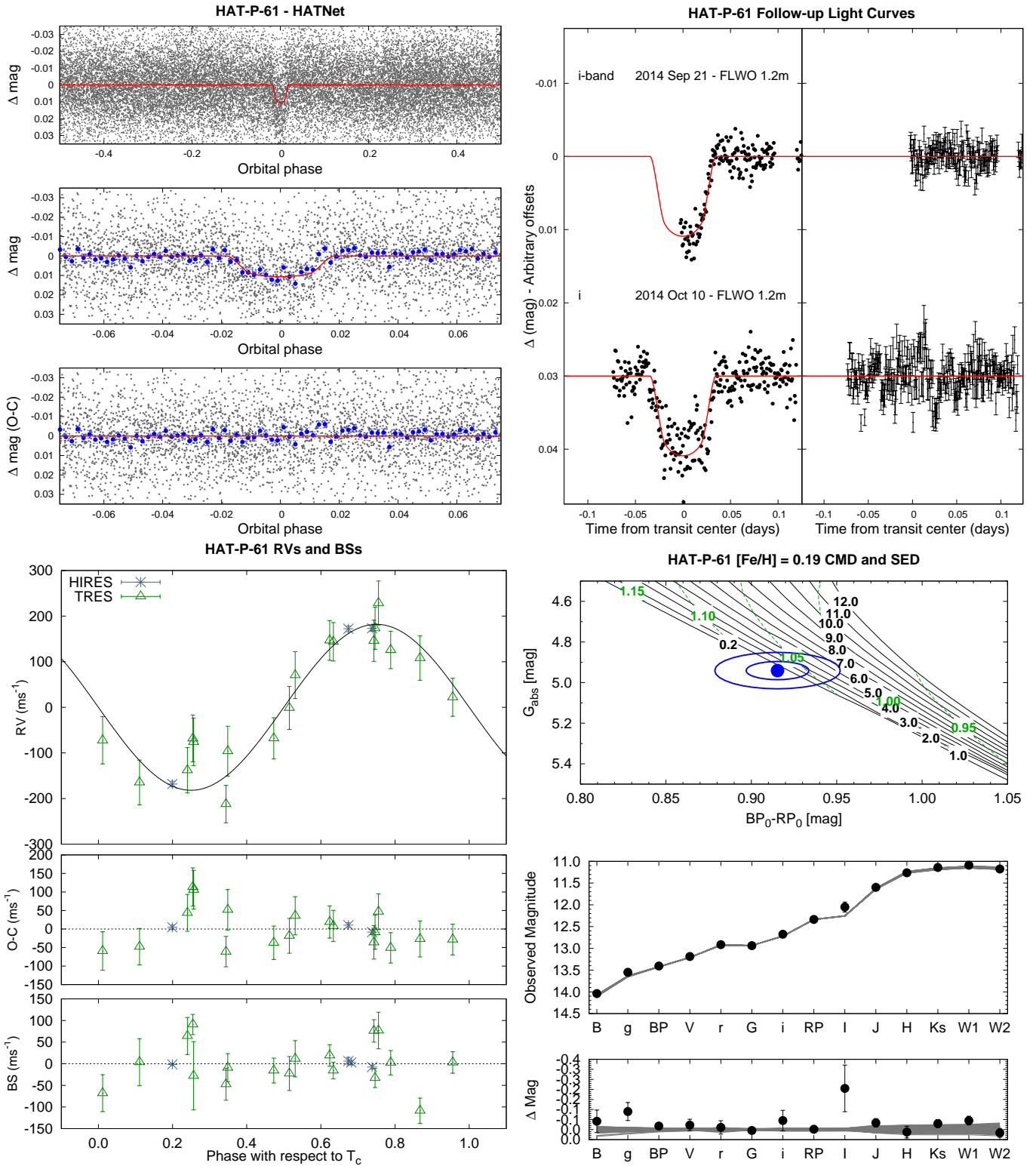## HAT-P-64 P=4.01d M$_P$=0.58M$_{Jup}$ R$_P$=1.70R$_{Jup}$ M$_S$=1.30M$_{Sun}$ R$_S$=1.73R$_{Sun}$
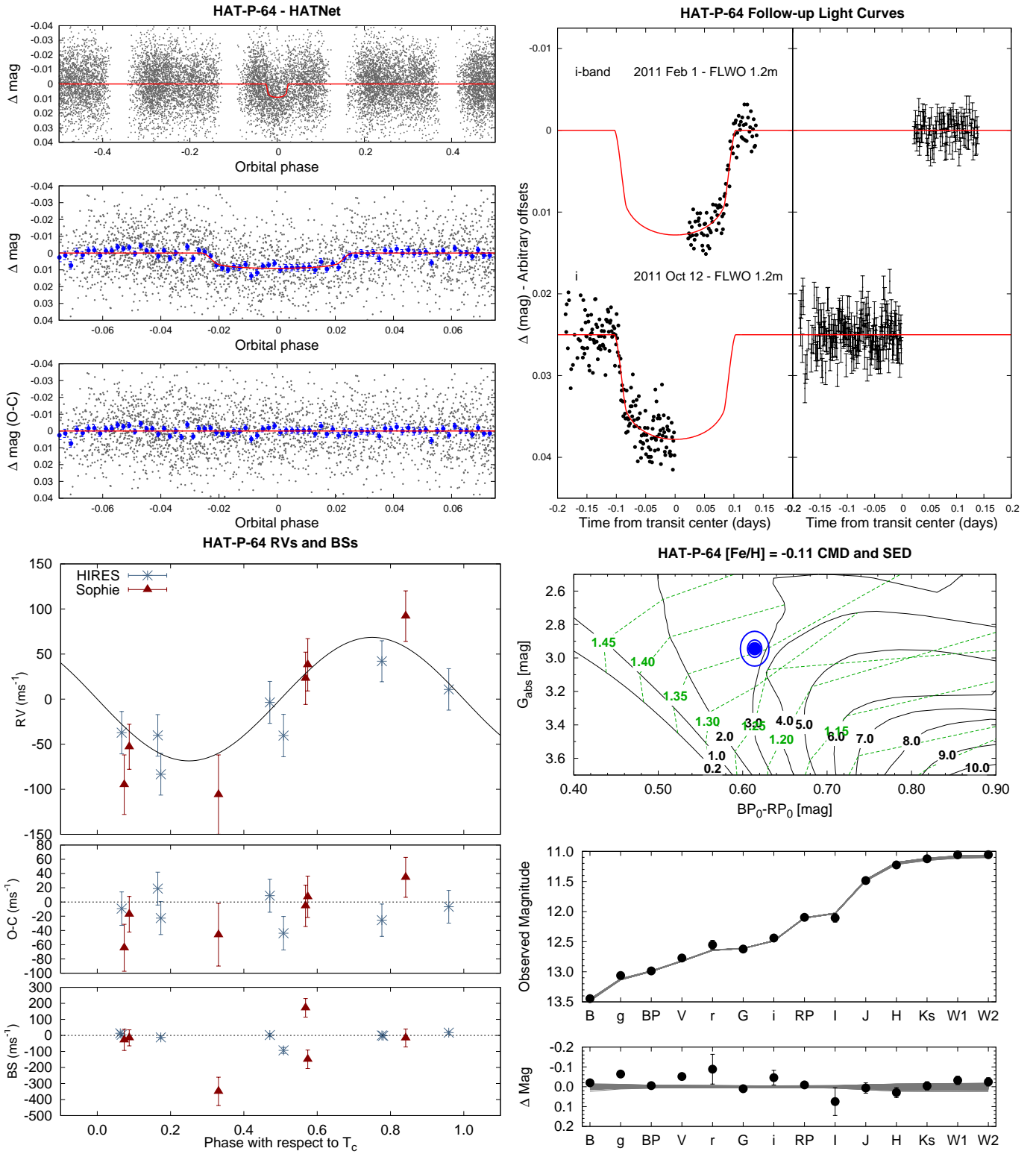
Figure 10. Observations of HAT-P-64 together with our best-fit model. Please refer to Figure 1 for a more detailed caption. The *TESS* light curve for this system is shown in Figure 14.

TESS Full Un-phased Light Curve of HAT-P-59

Full Phase-folded

Phase-folded Primary Transit

Phase-folded Secondary Eclipse

Phase-folded Primary Transit Residuals
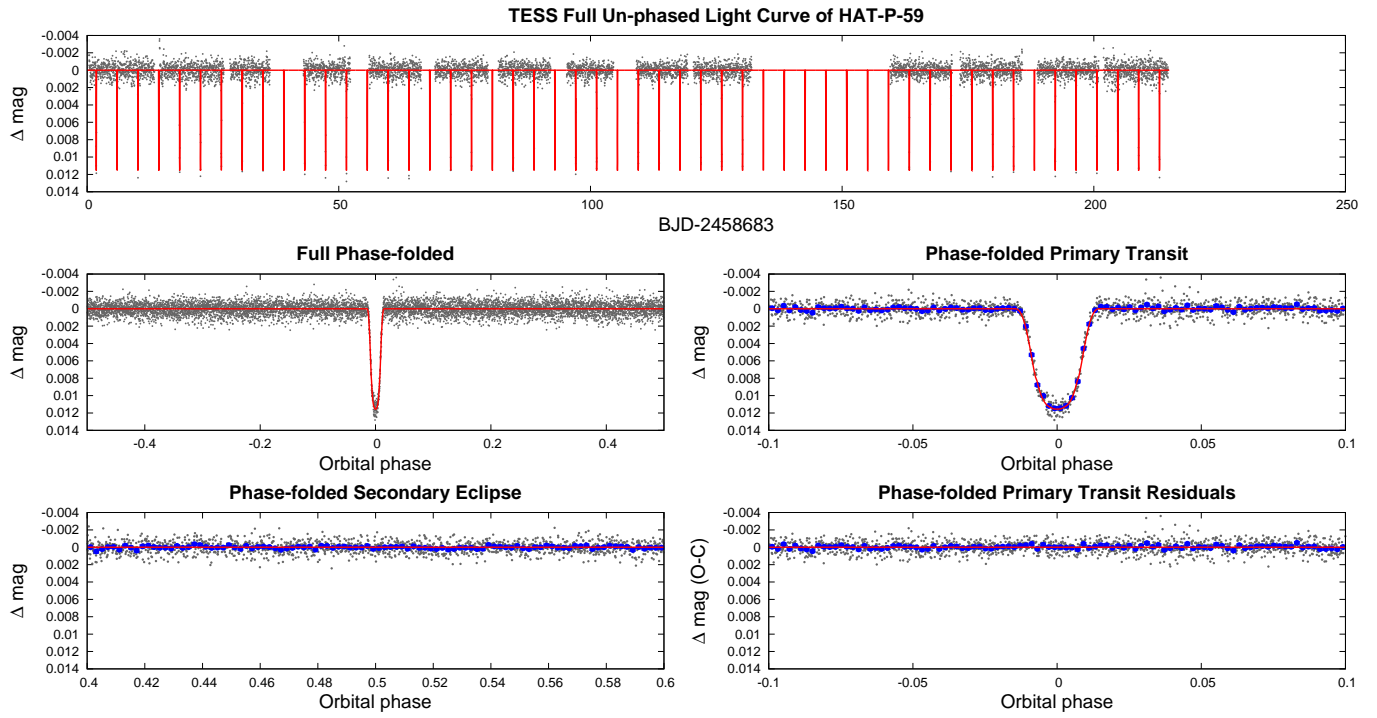
Figure 11. Similar to Figure 2, here we show the *TESS* long-cadence light curve for HAT-P-59. Other observations included in our analysis of this system are shown in Figure 5.

TESS Full Un-phased Light Curve of HAT-P-60

Full Phase-folded

Phase-folded Primary Transit

Phase-folded Secondary Eclipse

Phase-folded Primary Transit Residuals
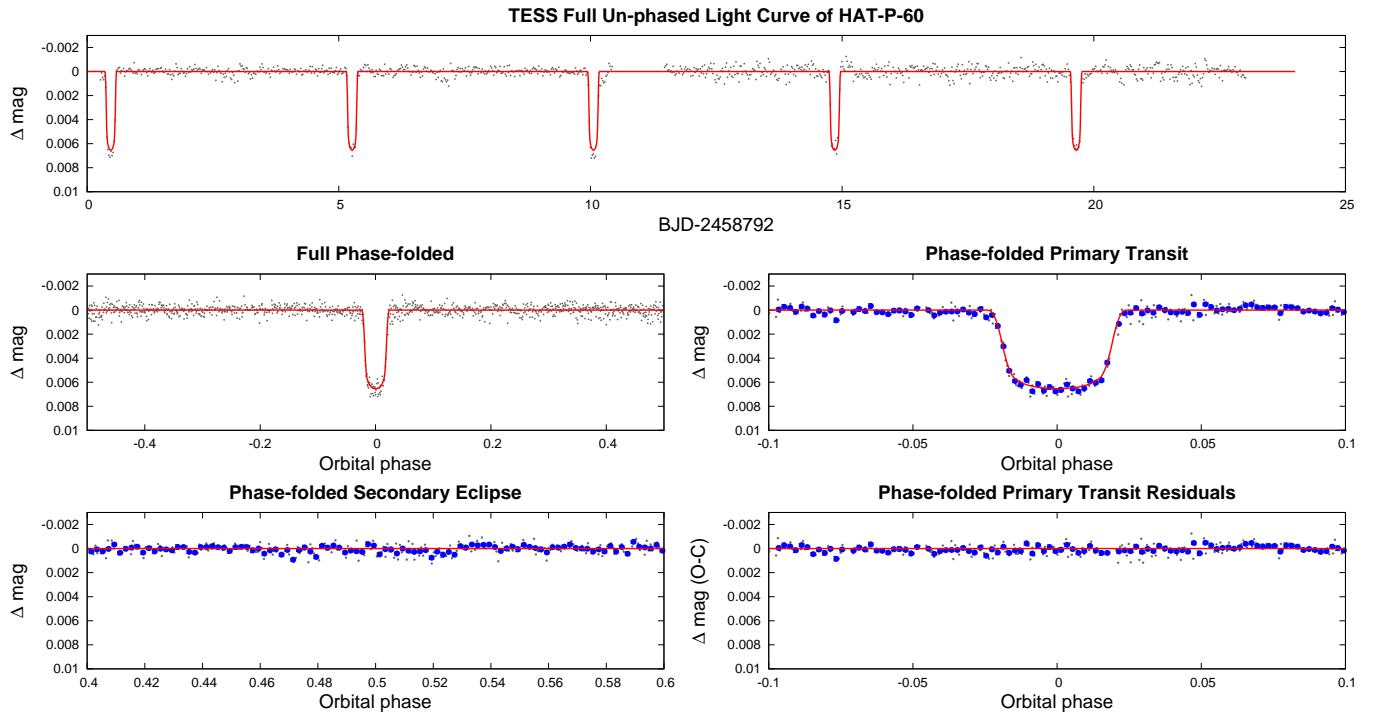
Figure 12. Similar to Figure 2, here we show the *TESS* long-cadence light curve for HAT-P-60. Other observations included in our analysis of this system are shown in Figure 6.

TESS Full Un-phased Light Curve of HAT-P-61
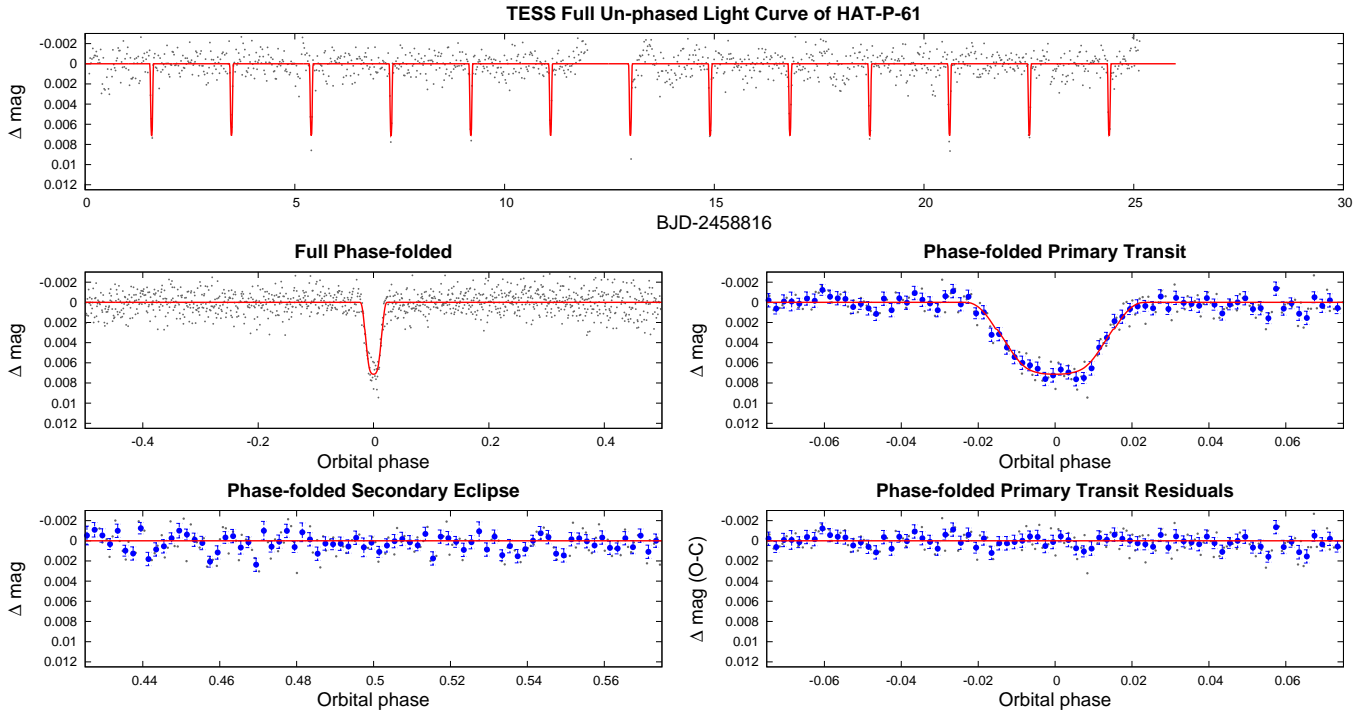
Figure 13. Similar to Figure 2, here we show the *TESS* long-cadence light curve for HAT-P-61. Other observations included in our analysis of this system are shown in Figure 7.

TESS Full Un-phased Light Curve of HAT-P-64
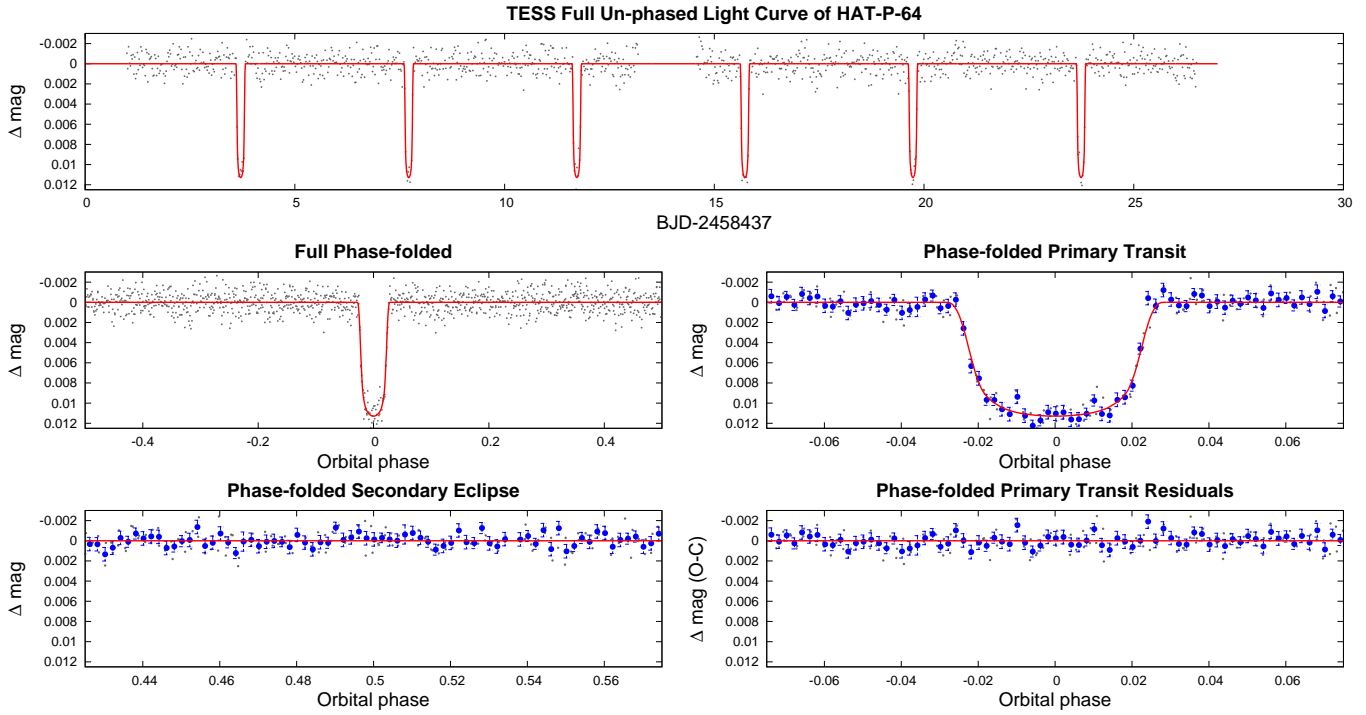
Figure 14. Similar to Figure 2, here we show the *TESS* long-cadence light curve for HAT-P-64. Other observations included in our analysis of this system are shown in Figure 10.
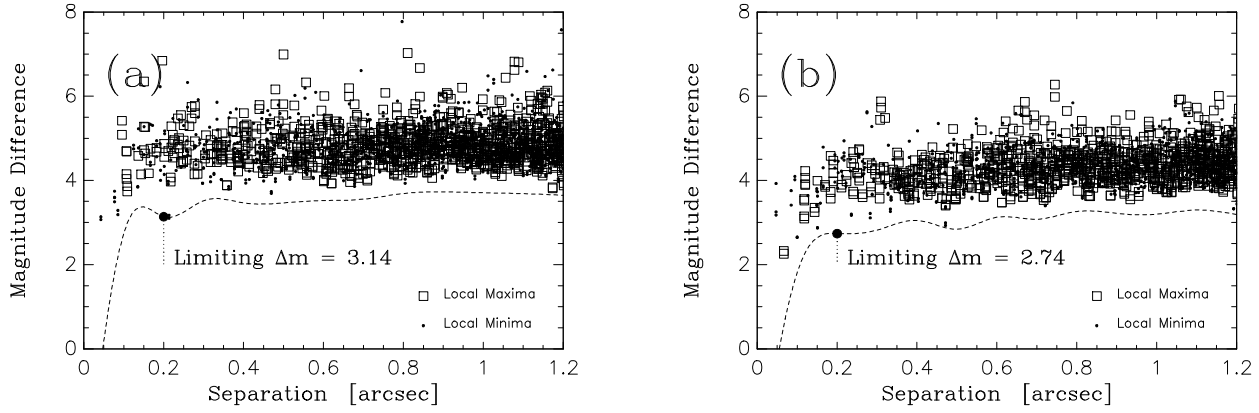
Figure 15. Same as Figure 4, here we show the results for HAT-P-59.
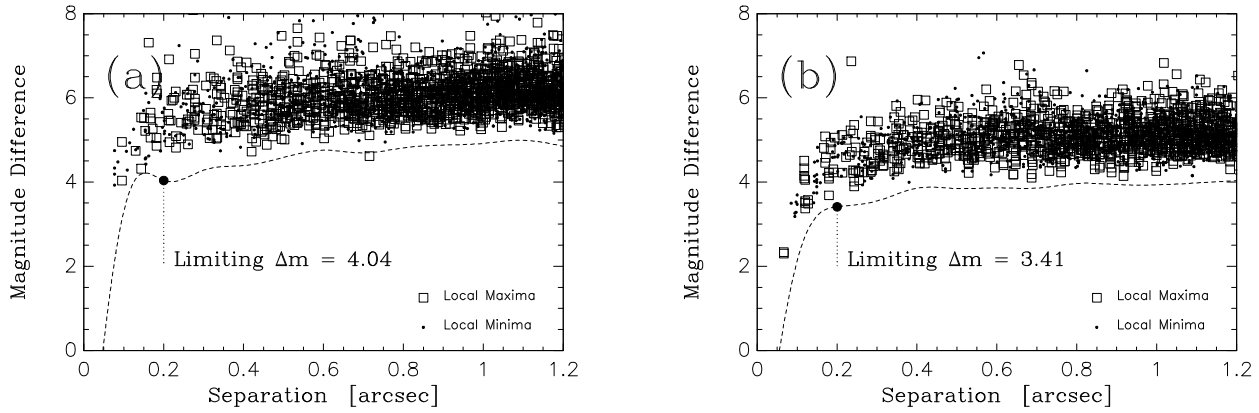
Figure 16. Same as Figure 4, here we show the results for HAT-P-60.
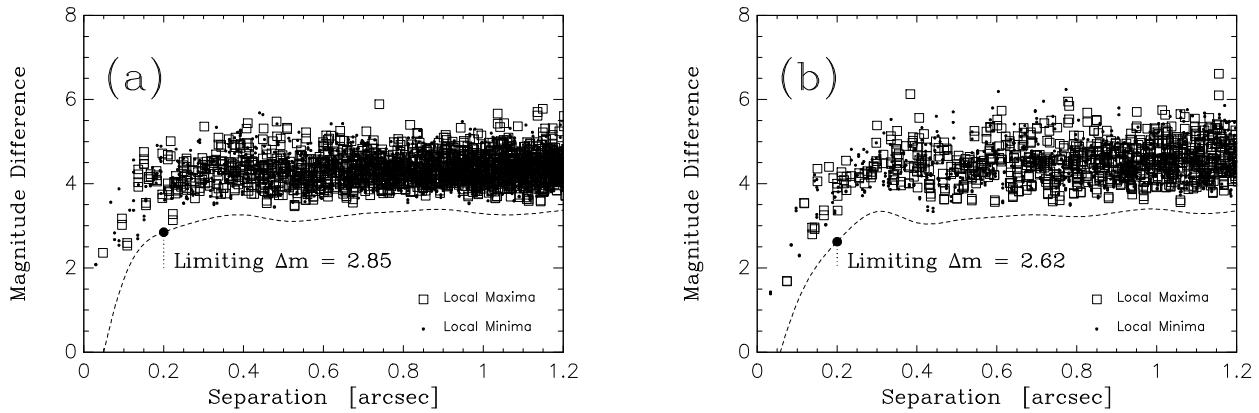
Figure 17. Same as Figure 4, here we show the results for HAT-P-61.
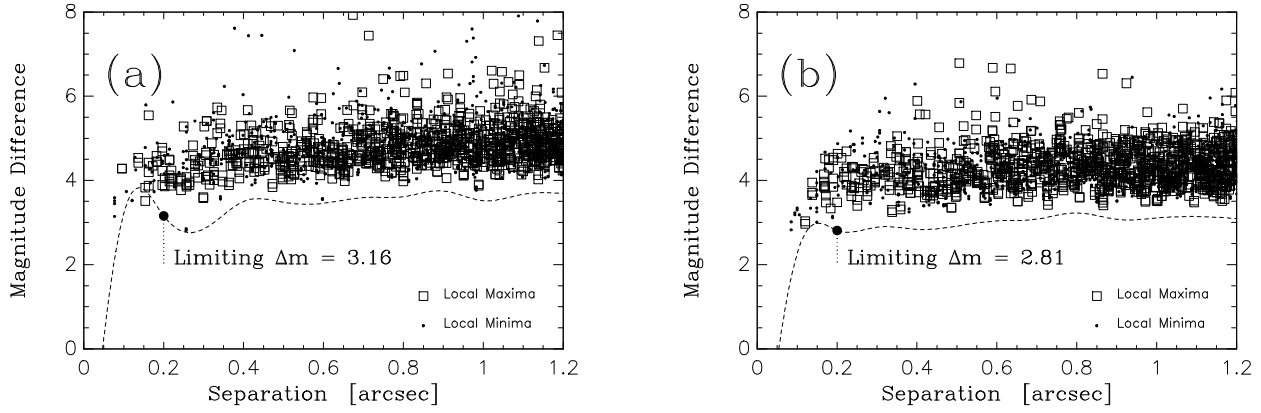
Figure 18. Same as Figure 4, here we show the results for HAT-P-62.

Figure 19. Similar to Figure 4, here we show the results for HAT-P-63 obtained with the NESSI instrument on the WIYN 3.5 m. For this instrument the filters used have wavelengths of 562 nm (left) and 832 nm (right).

Figure 20. Same as Figure 4, here we show the results for HAT-P-64.

Table 12. Relative radial velocities and bisector spans for HAT-P-58–HAT-P-64.

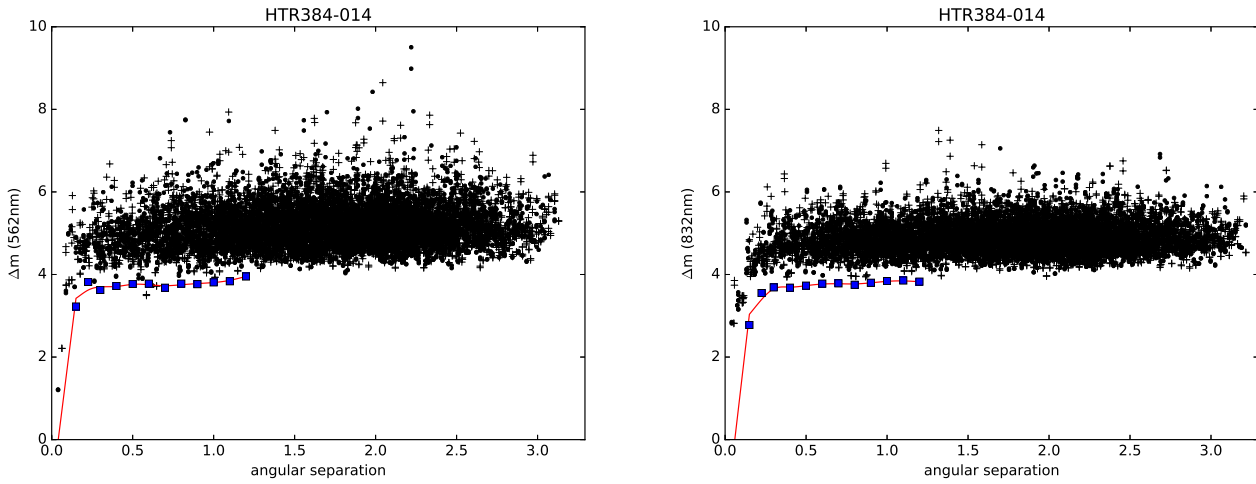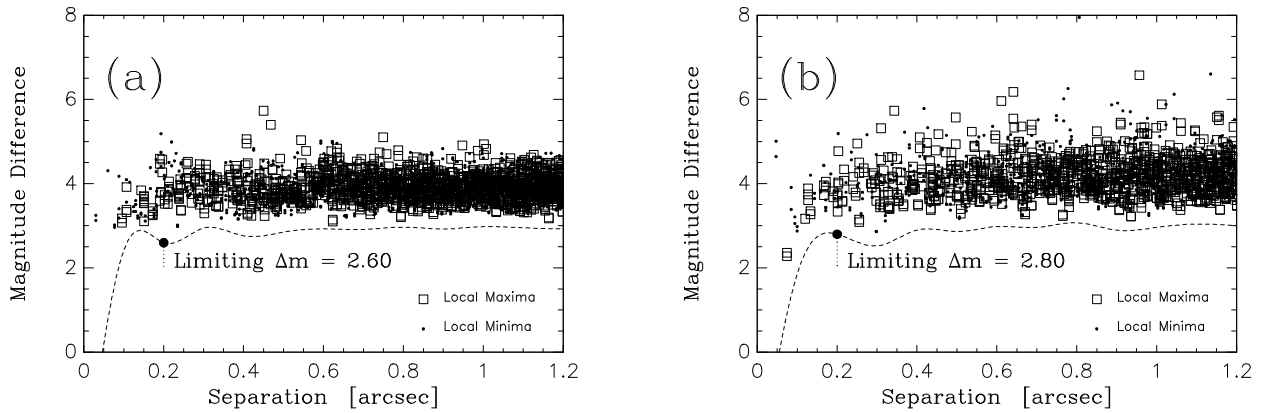| Star	BJD	RV[a]	$\sigma_{\rm RV}$[b]	BS	$\sigma_{\rm BS}$	$S_{\rm HK}$[c]	Phase	Instrument
	(2,450,000+)	$(\mathrm{m\,s^{-1}})$	$(\mathrm{m\,s^{-1}})$	$(\mathrm{m\,s^{-1}})$	$(\mathrm{m\,s^{-1}})$			
HAT-P-58								
HAT-P-58	6890.12499	40.53	7.42	33.5	20.2	0.172	0.686	HIRES
HAT-P-58	6892.12712	−46.48	2.99	−16.9	9.8	0.153	0.185	HIRES
HAT-P-58	6894.09295	36.41	2.71	−4.2	3.1	0.144	0.675	HIRES
HAT-P-58	6895.09290	$\cdots$	$\cdots$	−15.5	4.7	0.145	0.924	HIRES
HAT-P-58	6896.07796	−37.36	2.87	−14.6	5.6	0.142	0.169	HIRES
HAT-P-58	6909.10189	−20.66	3.83	13.6	15.5	0.157	0.414	HIRES
HAT-P-58	6910.07872	54.59	4.93	24.4	48.1	0.145	0.657	HIRES
HAT-P-58	6912.08980	−36.75	2.87	−20.4	8.0	0.143	0.158	HIRES
HAT-P-59								
HAT-P-59	6581.71540	−173.34	30.32	−8.1	16.1	0.248		TRES
HAT-P-59	6583.69510	222.45	26.21	14.5	9.7	0.726		TRES
HAT-P-59	6585.65905	−166.02	31.64	4.4	9.3	0.200		TRES
HAT-P-59	6593.29170	−42.34	11.50	−48.7	22.9	0.043		Sophie
HAT-P-59	6595.25025	51.96	36.10	−136.2	72.2	0.516		Sophie
HAT-P-59	6596.25559	214.46	14.70	−12.8	29.5	0.759		Sophie
HAT-P-59	6597.24301	−6.84	9.70	−44.5	19.5	0.997		Sophie
HAT-P-59	6598.26817	−164.04	31.80	−50.0	63.6	0.244		Sophie
HAT-P-59	6599.25285	−31.24	12.00	−22.5	24.0	0.482		Sophie
HAT-P-59	6599.26717	−32.54	21.10	−81.7	42.1	0.486		Sophie
HAT-P-59	6600.23567	218.06	21.10	46.2	42.2	0.719		Sophie
HAT-P-59	6601.31614	27.36	9.30	−29.2	18.5	0.980		Sophie
HAT-P-59	6602.30141	−195.44	14.40	−15.3	28.8	0.218		Sophie
HAT-P-59	6605.60024	−49.83	19.04	−27.6	7.9	0.015		TRES
HAT-P-59	6606.60413	−152.84	24.81	−3.4	24.4	0.257		TRES
HAT-P-59	6607.59892	−19.99	19.87	0.8	11.9	0.497		TRES
HAT-P-59	6608.60682	190.72	31.37	−4.0	13.8	0.740		TRES
HAT-P-59	6609.61035	27.93	18.27	31.0	13.6	0.983		TRES
HAT-P-59	6610.62724	−214.20	26.99	23.6	10.3	0.228		TRES
HAT-P-59	6611.59706	−3.09	21.75	18.0	17.5	0.462		TRES
HAT-P-59	6615.58195	−114.55	21.68	−1.0	9.4	0.425		TRES
HAT-P-59	6616.59129	144.92	12.85	−19.8	11.0	0.668		TRES
HAT-P-59	6617.62764	62.24	12.85	−28.4	10.4	0.918		TRES
HAT-P-60								
HAT-P-60	6326.58810	42.15	24.93	−18.2	15.9	$\cdots$	0.716	TRES
HAT-P-60	6549.78555	−57.10	47.30	24.4	31.6	$\cdots$	0.266	TRES
HAT-P-60	6551.82293	23.30	36.39	44.7	35.9	$\cdots$	0.691	TRES
HAT-P-60	6558.92278	−32.08	34.84	−51.5	28.6	$\cdots$	0.172	TRES
HAT-P-60	6573.89597	−44.23	19.98	15.3	10.0	$\cdots$	0.295	TRES
HAT-P-60	6574.90009	−41.76	24.66	4.4	14.1	$\cdots$	0.504	TRES
HAT-P-60	6575.79583	38.08	23.17	−16.4	15.2	$\cdots$	0.691	TRES
HAT-P-60	6576.77948	9.39	24.46	−1.6	17.9	$\cdots$	0.896	TRES
HAT-P-60	6577.80537	−33.50	24.93	−3.6	31.4	$\cdots$	0.110	TRES
HAT-P-60	6578.74876	−61.26	18.25	−7.1	14.2	$\cdots$	0.307	TRES
HAT-P-60	6580.72123	66.89	18.25	5.2	14.7	$\cdots$	0.718	TRES

Table 12 *continued*

Table 12 *(continued)*

Star	BJD	RV[a]	$\sigma_{\rm RV}$[b]	BS	$\sigma_{\rm BS}$	S$_{\rm HK}$[c]	Phase	Instrument
	(2,450,000+)	(m s^{-1})	(m s^{-1})	(m s^{-1})	(m s^{-1})			
HAT-P-60	6581.79896	32.21	21.62	13.8	14.6	$\cdots$	0.943	TRES
HAT-P-60	6582.85746	−63.67	21.79	−9.5	11.2	$\cdots$	0.164	TRES
HAT-P-60	6593.49292	−16.13	32.40	−82.7	64.8	$\cdots$	0.382	Sophie
HAT-P-60	6595.51401	32.07	27.10	−54.7	54.1	$\cdots$	0.803	Sophie
HAT-P-60	6596.66289	−15.03	22.50	28.5	45.0	$\cdots$	0.043	Sophie
HAT-P-60	6597.40379	−27.23	22.30	−23.5	44.6	$\cdots$	0.197	Sophie
HAT-P-60	6599.55850	35.07	14.40	−74.3	28.8	$\cdots$	0.647	Sophie
HAT-P-60	6600.53433	45.07	26.20	−38.2	52.3	$\cdots$	0.850	Sophie
HAT-P-60	6601.63510	−28.93	22.50	15.5	45.0	$\cdots$	0.080	Sophie
HAT-P-60	6602.40299	−67.13	15.10	−10.2	30.2	$\cdots$	0.240	Sophie
HAT-P-60	6637.75333	29.51	3.22	6.3	3.2	0.121	0.613	HIRES
HAT-P-60	6638.81890	33.03	4.25	0.3	2.8	0.123	0.835	HIRES
HAT-P-60	7353.80988	36.33	4.11	−8.1	5.4	0.124	0.954	HIRES
HAT-P-60	7354.79800	−40.93	3.99	8.4	4.5	0.124	0.160	HIRES
HAT-P-60	7355.79193	−21.46	3.78	−0.8	3.7	0.123	0.367	HIRES
HAT-P-60	7355.89024	$\cdots$	$\cdots$	−7.1	4.1	0.122	0.387	HIRES
HAT-P-60	7378.72938	−26.21	4.10	−0.3	3.6	0.126	0.151	HIRES
HAT-P-60	7401.88232	22.14	4.50	10.4	4.5	0.121	0.980	HIRES
HAT-P-60	7412.79458	−58.33	4.40	−9.1	3.5	0.128	0.255	HIRES

HAT-P-61

Star	BJD	RV	$\sigma_{\rm RV}$	BS	$\sigma_{\rm BS}$	S$_{\rm HK}$	Phase	Instrument
HAT-P-61	6910.98025	149.18	26.04	76.1	25.9	$\cdots$	0.743	TRES
HAT-P-61	6911.92592	−134.70	33.23	64.2	42.9	$\cdots$	0.241	TRES
HAT-P-61	6912.96888	129.17	17.84	2.4	28.1	$\cdots$	0.789	TRES
HAT-P-61	6931.91154	176.60	27.60	−32.9	22.0	$\cdots$	0.747	TRES
HAT-P-61	6932.88321	−72.55	36.71	−27.9	78.9	$\cdots$	0.257	TRES
HAT-P-61	6934.95150	−208.83	17.84	−47.2	37.0	$\cdots$	0.345	TRES
HAT-P-61	6935.94714	111.18	31.50	−108.5	29.2	$\cdots$	0.868	TRES
HAT-P-61	6944.99515	149.97	22.95	19.2	24.9	$\cdots$	0.624	TRES
HAT-P-61	6945.92201	−161.35	32.35	3.7	54.5	$\cdots$	0.112	TRES
HAT-P-61	6958.94233	25.21	19.23	3.0	24.8	$\cdots$	0.956	TRES
HAT-P-61	6960.00651	2.01	29.22	−22.6	39.3	$\cdots$	0.515	TRES
HAT-P-61	6960.95084	−69.03	36.34	−68.0	42.7	$\cdots$	0.012	TRES
HAT-P-61	6961.93882	73.86	35.83	11.5	41.9	$\cdots$	0.531	TRES
HAT-P-61	6965.93914	146.95	20.19	−15.7	19.3	$\cdots$	0.634	TRES
HAT-P-61	6970.92528	−64.93	35.63	90.8	23.4	$\cdots$	0.255	TRES
HAT-P-61	6971.87773	232.02	31.09	76.8	42.3	$\cdots$	0.756	TRES
HAT-P-61	6973.00690	−92.82	40.13	−9.2	32.6	$\cdots$	0.349	TRES
HAT-P-61	6978.94963	−64.74	25.97	−15.7	28.7	$\cdots$	0.473	TRES
HAT-P-61	7354.08818	169.27	1.12	6.1	8.8	0.258	0.675	HIRES
HAT-P-61	7355.08733	−171.23	0.90	−1.5	2.5	0.232	0.200	HIRES
HAT-P-61	7356.00551	$\cdots$	$\cdots$	2.9	4.8	0.232	0.682	HIRES
HAT-P-61	7356.11208	170.17	0.86	−7.5	4.7	0.237	0.738	HIRES

HAT-P-62

Star	BJD	RV	$\sigma_{\rm RV}$	BS	$\sigma_{\rm BS}$	S$_{\rm HK}$	Phase	Instrument
HAT-P-62	6674.65588	−126.65	21.61	30.9	29.2	0.258	TRES	
HAT-P-62	6707.64331	88.60	25.94	−13.4	27.3	0.728	TRES	
HAT-P-62	6942.95953	148.33	23.82	−47.5	32.3	0.683	TRES	
HAT-P-62	6945.86085	164.72	17.63	11.1	34.1	0.780	TRES	
HAT-P-62	6958.92253	74.01	19.07	−15.2	18.8	0.718	TRES	
HAT-P-62	6959.99100	−30.23	26.36	1.3	27.9	0.121	TRES	

Table 12 *continued*

Bakos et al.

Table 12 *(continued)*

Star	BJD	RV[a]	σ_{RV}[b]	BS	σ_{BS}	S$_{HK}$[c]	Phase	Instrument
	(2,450,000+)	(m s^{-1})	(m s^{-1})	(m s^{-1})	(m s^{-1})			
HAT-P-62	6960.93014	-1.99	20.56	-15.8	20.6	0.476	TRES	
HAT-P-62	6961.91630	33.97	16.43	24.2	21.0	0.849	TRES	
HAT-P-62	6962.86334	-108.71	17.73	52.5	24.9	0.207	TRES	
HAT-P-62	6965.87438	-126.58	14.60	0.6	24.2	0.346	TRES	
HAT-P-62	6970.87354	-45.58	22.84	-75.3	48.3	0.235	TRES	
HAT-P-62	6971.83494	56.80	18.00	5.3	24.7	0.599	TRES	
HAT-P-62	6972.87045	2.71	23.65	-30.3	23.0	0.990	TRES	
HAT-P-62	6977.88426	84.76	27.25	52.8	26.9	0.886	TRES	
HAT-P-62	6978.92626	-134.32	14.60	18.9	25.0	0.279	TRES	
HAT-P-63								
HAT-P-63	6023.91391	129.50	38.60	0.0	0.0	0.707	TRES	
HAT-P-63	6045.89542	-84.12	38.60	0.0	-427.2	0.215	TRES	
HAT-P-63	6189.73983	$\cdots$	$\cdots$	-4.9	19.9	0.801	HDS	
HAT-P-63	6189.75456	$\cdots$	$\cdots$	-9.9	20.4	0.805	HDS	
HAT-P-63	6189.76928	$\cdots$	$\cdots$	-5.0	22.9	0.810	HDS	
HAT-P-63	6189.78400	$\cdots$	$\cdots$	-9.1	22.6	0.814	HDS	
HAT-P-63	6190.73339	-54.82	7.80	-1.0	23.4	0.095	HDS	
HAT-P-63	6190.74813	-54.06	7.84	13.8	18.3	0.100	HDS	
HAT-P-63	6190.76286	-58.71	8.10	10.1	16.5	0.104	HDS	
HAT-P-63	6190.77762	-58.26	7.29	4.0	17.5	0.108	HDS	
HAT-P-63	6191.73872	-53.97	12.13	11.2	8.7	0.393	HDS	
HAT-P-63	6191.75344	-47.95	10.48	-7.7	9.0	0.397	HDS	
HAT-P-63	6191.76817	-49.52	13.25	15.8	12.8	0.402	HDS	
HAT-P-63	6191.78289	-62.43	12.27	32.1	14.5	0.406	HDS	
HAT-P-63	6192.73493	79.05	8.31	-14.2	18.9	0.688	HDS	
HAT-P-63	6192.74967	80.64	7.60	-4.2	12.3	0.692	HDS	
HAT-P-63	6192.76439	80.82	8.44	-16.0	17.3	0.697	HDS	
HAT-P-63	6192.77911	77.11	8.65	-14.9	15.3	0.701	HDS	
HAT-P-63	6446.51381	54.19	18.60	-51.2	37.2	0.821	Sophie	
HAT-P-63	6447.50510	-35.01	12.50	-6.5	25.0	0.114	Sophie	
HAT-P-63	6448.56434	-37.31	13.10	-5.8	26.2	0.428	Sophie	
HAT-P-63	6449.56056	45.69	14.70	-36.7	29.4	0.723	Sophie	
HAT-P-63	6451.51641	-100.41	11.30	-15.0	22.6	0.302	Sophie	
HAT-P-63	6454.53652	-72.61	12.20	-77.2	24.4	0.196	Sophie	
HAT-P-63	6456.50551	103.69	8.20	-21.7	16.4	0.779	Sophie	
HAT-P-64								
HAT-P-64	5611.85377	$\cdots$	$\cdots$	13.3	8.1	0.159	0.063	HIRES
HAT-P-64	5611.86923	-27.85	8.60	3.8	8.4	0.140	0.067	HIRES
HAT-P-64	5815.07604	51.41	6.24	-0.1	8.1	0.141	0.777	HIRES
HAT-P-64	5815.08975	$\cdots$	$\cdots$	-2.4	6.2	0.140	0.781	HIRES
HAT-P-64	5853.92294	5.75	7.85	2.3	9.6	0.137	0.471	HIRES
HAT-P-64	5879.92287	20.12	6.98	17.1	9.6	0.148	0.960	HIRES
HAT-P-64	5882.12309	-31.01	8.59	-93.6	18.5	0.151	0.509	HIRES
HAT-P-64	5901.44866	-93.15	44.00	-349.0	88.0	$\cdots$	0.331	Sophie
HAT-P-64	5902.42391	50.85	29.00	-149.0	58.0	$\cdots$	0.575	Sophie
HAT-P-64	5903.49529	104.85	28.00	-16.0	56.0	$\cdots$	0.842	Sophie
HAT-P-64	5904.47960	-40.15	25.00	-15.0	50.0	$\cdots$	0.088	Sophie
HAT-P-64	5904.79205	-30.84	7.20	$\cdots$	$\cdots$	$\cdots$	0.166	HIRES
HAT-P-64	5906.40764	35.85	29.00	172.0	58.0	$\cdots$	0.569	Sophie

Table 12 *continued*